Materials Advances

PAPER

View Article Online
View Journal | View Issue

Cite this: *Mater. Adv.*, 2024, **5**, 3228

3D printed bioactive calcium silicate ceramics as antibacterial scaffolds for hard tissue engineering†

Joelle El Hayek,[ab] Habib Belaid,[a] Louis Cornette de Saint Cyr,[a] Ghenwa El Chawich,[ab] Emerson Coy,[c] Igor Iatsunskyi,[c] Christel Gervais,[d] Jeevithan Elango,[e] Camilo Zamora-Ledezma,[f] Mikhael Bechelany,[ag] Michel Nakhl,[b] Damien Voiry,[a] Philippe Miele,[ah] Mirvat Zakhour,[b] Laurence Soussan[a] and Chrystelle Salameh*[a]

VAT photopolymerization technology was applied to fabricate three-dimensional (3D) porous β-Ca_2SiO_4 ceramic scaffolds functionalized with graphene oxide (GO) sheets decorated with silver nanoparticles (AgNPs). We achieved this by utilizing commercial resin blends and "customized" resin both loaded with $CaCO_3$ particles. The dual functionality of the "customized" resin, which serves as both a preceramic polymer and photocurable resin, is exploited. To assess the properties of these ceramics, we carried out an in-depth comparative analysis using a combination of spectroscopic, microscopic and analytical techniques. After annealing at 1200 °C, the as-prepared ceramics achieved a relative density of 65% leading to high compressive strength ($\approx$40 MPa). Importantly, β-Ca_2SiO_4 ceramic scaffolds demonstrated good *in vitro* bioactivity by promoting hydroxyapatite formation. When subjected to *E. coli*, scaffolds functionalized with AgNPs/GO showed higher antibacterial activity than their non-functionalized counterparts. Moreover, ceramic scaffolds derived from the "customized" resin exhibited sixfold higher antimicrobial activity than scaffolds made from commercial resin mixtures. To assess biocompatibility, we conducted *in vitro* studies using mesenchymal stem cells (MSCs) culture. Encouragingly, all bioceramics proved non-cytotoxic and accelerated the proliferative rate of MSCs compared with the control. After 7 days in culture, cells showed a well-spread morphology with no obvious differences, clearly indicating that bioceramic scaffolds actively promote cell adhesion and viability. Overall, due to their interconnected porosity, excellent biomineralization, mechanical, antibacterial and cytocompatibility properties, these 3D-printed scaffolds hold significant promise as candidates for applications in hard tissue engineering.

Received 6th December 2023,
Accepted 23rd February 2024

DOI: 10.1039/d3ma01088k

rsc.li/materials-advances

1. Introduction

Over the last five decades, a remarkable revolution has taken place in the use of ceramics, significantly improving our quality of life. This transformation is closely linked to the innovative use of ceramics specifically designed for the repair and reconstruction of diseased or damaged body parts. Ceramics used for this purpose are commonly referred to as bioceramics.[1,2] Bioceramics are widely used in hard tissue engineering, mainly due to their biocompatibility and adjustable properties. However, they often exhibit limited antibacterial activity. Infections at the implant site can potentially impede the bone healing process, leading to implant failure.[3,4] Many scaffolds that have proved highly effective *in vitro* have failed in *in vivo* experiments and human trials due to severe infections, and the implant often has to be surgically removed.[5,6] Indeed, as the literature shows, the growth of bacterial infections is controlled by the surface properties and composition of biomaterials. This is why

---

[a] *Institut Européen des Membranes, IEM, UMR 5635, University Montpellier, ENSCM, CNRS, Montpellier, Cedex 5 34095, France. E-mail: joelle-hayek@hotmail.com, chrystelle.salameh@umontpellier.fr*
[b] *Laboratoire de Chimie Physique des Matériaux/Plateforme de Recherche en Nanomatériaux et Nanotechnologies (LCPM/PR2N), Lebanese University, Beirut 90656, Lebanon*
[c] *NanoBioMedical Centre, Adam Mickiewicz University, Wszechnicy Piastowksiej str. 3, Poznan 61-614, Poland*
[d] *Sorbonne Université, UMR 7574 CNRS, Laboratoire de Chimie de la Matière Condensée de Paris, LCMCP, Paris F-75005, France*
[e] *Department of Biomaterials Engineering, Faculty of Health Sciences, UCAM-Universidad Católica San Antonio de Murcia, Campus de los Jerónimos 135, Guadalupe, Murcia 30107, Spain*
[f] *Green and Innovative Technologies for Food, Environment and Bioengineering Research Group (FEnBeT), Faculty of Pharmacy and Nutrition, UCAM-Universidad Católica San Antonio de Murcia, Campus de los Jerónimos 135, Guadalupe, Murcia 30107, Spain*
[g] *Gulf University for Science and Technology, GUST, Kuwait*
[h] *Institut Universitaire de France (IUF), Paris, France*

† Electronic supplementary information (ESI) available. See DOI: https://doi.org/10.1039/d3ma01088k

it is of great interest today to develop new antibacterial and biocompatible bioceramics with good mechanical and microstructural properties.[7–9] Calcium silicate-based bioactive ceramic scaffolds are of particular interest due to their bioactivity, biocompatibility and osteoinductive capabilities, as well as their promotion of cell adhesion, proliferation and differentiation.[10–15] Compared to Ca–P-based bioceramics, silicon (Si) plays an essential role in mineralization and gene activation in the bone regeneration process,[16] but manufacturing Si-based ceramics with complex geometries close to net shape is difficult. To date, silicate bioceramics, such as wollastonite ($CaSiO_3$), diopside ($CaMgSi_2O_6$), akermanite ($Ca_2MgSi_2O_7$), hardystonite ($Ca_2ZnSi_2O_7$) and bredigite ($Ca_7MgSi_4O_{16}$) have been fabricated as three dimensional (3D) porous scaffolds for bone tissue engineering applications.[12,17–24]

β-Ca_2SiO_4 ceramic represents a new class of silica-based ceramics known for their bioactive properties, capable of inducing the formation of a hydroxyapatite (HAP) layer on the surface when exposed to physiological media like Simulated Body Fuids (SBF).[25] Dail *et al.* prepared porous β-Ca_2SiO_4 ceramic scaffolds using a modified sponge impregnation technique (polyurethane foam) with compressive strengths of 28 MPa and 10 MPa at 53% and 71% porosity respectively with good biocompatibility and excellent biomineralization.[26] Choudhary *et al.* prepared porous β-Ca_2SiO_4 and β-Ca_2SiO_4/chitin scaffolds to study the effect of polymer content on the bioactivity of composites in SBF using the porogen templating technique. They demonstrated that increasing the polymer composition in the ceramic matrix increases the scaffold's HAP layer formation capacity.[27] Indeed, the main drawback of these conventional methods of fabricating porous scaffolds lies in the fact that the pores are not uniform and interconnected, resulting in poor mechanical behavior and inefficient cell growth and nutrient transport.[28,29] Ideally, the scaffold structure should be porous, with open interconnected pores to provide sufficient space for cell adhesion and extracellular matrix regeneration.[30,31] To better control the morphology and size of pores and porosity, additive manufacturing has been used to prepare porous silicate scaffolds.[32–35] The significant advantage of 3D printing is that the scaffold architecture can be concisely controlled. For example, Fu *et al.* fabricated porous 3D β-Ca_2SiO_4 scaffolds with uniform interconnected macropores, high porosity (>78%) and compressive strength of 5.2 MPa for scaffolds sintered at 1200 °C from $CaCO_3$-filled preceramic silicone resin by direct ink 3D printing.[36,37] The authors show that increasing the sintering temperature significantly increases the compressive strength of the scaffold and also stimulates adhesion, proliferation, alkaline phosphatase (ALP) activity and osteogenesis-related gene expression in rat bone marrow mesenchymal stem cells (rBMSCs).[36,37] Similarly, β-Ca_2SiO_4 scaffolds derived from a silicone resin loaded with ZrO_2 as passive fillers and $CaCO_3$ as active fillers have already been produced by direct ink 3D printing. In this case, the incorporation of ZrO_2 improves compressive strength (up to 6.1 MPa), and also stimulates cell attachment, proliferation, and differentiation into osteoblasts.[36,37] Yu *et al.* prepared β-Ca_2SiO_4 scaffolds with aluminum ions using a preceramic resin, active $CaCO_3$ and Al_2O_3 powders by direct ink 3D printing. Aluminum incorporation improves proliferation and expression levels of osteogenic genes (osteocalcin, osteopontin, Collagen type I, and Runx2) of rBMSCs.[38] However, 3D printing with direct ink has drawbacks such as lack of precision in droplets size and placement as well as frequent nozzle clogging and cell distortion.[5,34,35] It is also necessary to use low-viscosity bioinks, which eliminates the use of several effective bioinks with this method. Indeed, ink for inkjet printing must be well formulated without agglomerates or aggregates to avoid any risk of clogging during printing.[39] To overcome these drawbacks, other techniques have been successfully explored, notably UV-LCD 3D printing, based on the layer-by-layer construction of objects by photopolymerization of a liquid resin contained in a tank and cured against a building platform. Thanks to the high resolution of the light source, it offers a better-quality printing surface, resulting in lower layer thickness, more detailed information and better surface quality.[40,41] Numerous bioceramics have also been successfully obtained using stereolithography 3D printing (SLA). Baino *et al.* prepared porous scaffolds by mixing hydroxyapatite (HAP) powder and a photocurable binder matrix containing acrylate- and methacrylate-based reactive monomers using digital light processing (DLP) 3D printing. These porous HAP scaffolds reproduce the open-cell 3D architecture of cancellous bone, with a compressive strength of $\sim$1.60 MPa and an elastic modulus of $\sim$513 MPa.[42–49] Similarly, Bian *et al.* prepared porous scaffolds by mixing β-TCP nanoparticles with a photosensitive resin based on acrylamide (AM) and methylene bisacrylamide (MBAM) using stereolithography. The authors show that the final ceramic scaffolds remain identical to the fabricated part, both in shape and internal structure, with a compressive strength of 23.54 MPa.[50–52] Chen *et al.* prepared bioceramic scaffolds by mixing ceramic powders (ZrO_2–Al_2O_3) with a photosensitive resin (1,6-hexanediol diacrylate – HDDA) using the stereolithography technique. According to their results, when the sintering temperature is increased from 1450 °C to 1600 °C, the average relative density, Vickers hardness, and fracture toughness all reach their maximum values (99.09%, 16.66 GPa, and 6.88 MPa $m^{1/2}$). The authors also demonstrated that ZrO_2–Al_2O_3 bioceramics prepared by SLA technology are not cytotoxic and have excellent biocompatibility.[53] Similarly, Lu *et al.* prepared porous calcium silicate scaffolds using SLA by mixing CSi–Mg6 bioceramic powder with a photosensitive resin (HDDA and pentaerythritol tetraacrylate PPTTA). They printed several shapes with different pore architectures and tested their influence on mechanical strength.[54,55] For their part, Schmidt *et al.* prepared porous ollastonite-diopside glass scaffolds by mixing glass particles with an acrylated polymer (tripropylene glycol diacrylate – TPGDA) using a DLP-based method. After sintering, they obtained porous Kelvin-type structures with compressive strength exceeding 3 MPa.[56,57] It is worth noting that SLA 3D printing of ceramics and glasses is not an easy process compared to that of polymer resins, as light is scattered by the ceramic particles, leading to printing problems that can affect the resolution of the printed scaffold. In addition, particles must be well dispersed and stabilized to avoid sedimentation and phase separation.[58–60] Silicate-based 3D printed bioceramics (using forsterite, β-TCP, hardystonite, diopside) have revealed antibacterial properties against *S. aureus*, *S. epidermidis* and *E. coli*.[61–65] However, to the best of our knowledge, neither β-Ca_2SiO_4 bioceramic fabricated by UV-LCD from a mixture of light-sensitive preceramic polymer resins nor its antibacterial activities have been reported to date.

Building on the above concept, this study presents an innovative approach to the fabrication of porous β-Ca_2SiO_4 scaffolds by UV-LCD, using two different preceramic resins. The first method involves mixing a commercially available methyl silicone resin with a photosensitive resin. The second method involves the synthesis of a ''customized'' photosensitive silicone resin. 3D scaffolds are obtained by printing these resins loaded with $CaCO_3$ particles. Then, the green bodies are subjected to sintering at 1200 °C in an inert atmosphere, leading to the formation of porous β-Ca_2SiO_4 scaffolds. These scaffolds are subsequently functionalized with silver nanoparticles (AgNPs) decorated with graphene oxide (GO) to achieve antibacterial activity. The present study further explores aspects such as biomineralization, dissolution, mechanical testing, antibacterial activity against *E. coli* bacteria and *in vitro* assessments of cytotoxicity and biocompatibility using a primary culture of adult human bone marrow-derived multipotent mesenchymal stem cells (ah-BM-MSCs) (Fig. 1).

2. Experimental procedures

2.1. Materials

A commercial methyl silicone resin (Silres® MK) was purchased from Wacker Chemie (Munich, Germany). Calcium carbonate ($CaCO_3$, ≥99%, CAS Number: 471-34-1), isopropyl alcohol (IPA, Bio Reagent, ≥99.5%, CAS Number: 67-63-0) and toluene (anhydrous, 99.8%, CAS Number: 108-88-3) were purchased from Sigma Aldrich, France. Commercial Polylactic Acid (PLA) Bio-photopolymer resin (d = 1.07–1.13 g cm^{-3}) was purchased from eSUN China.

For the ''customized'' synthesis of the photosensitive silicone resin, the polymer precursors (3-(trimethoxysilyl)propyl methacrylate, 98%, Sigma Aldrich France, CAS Number:

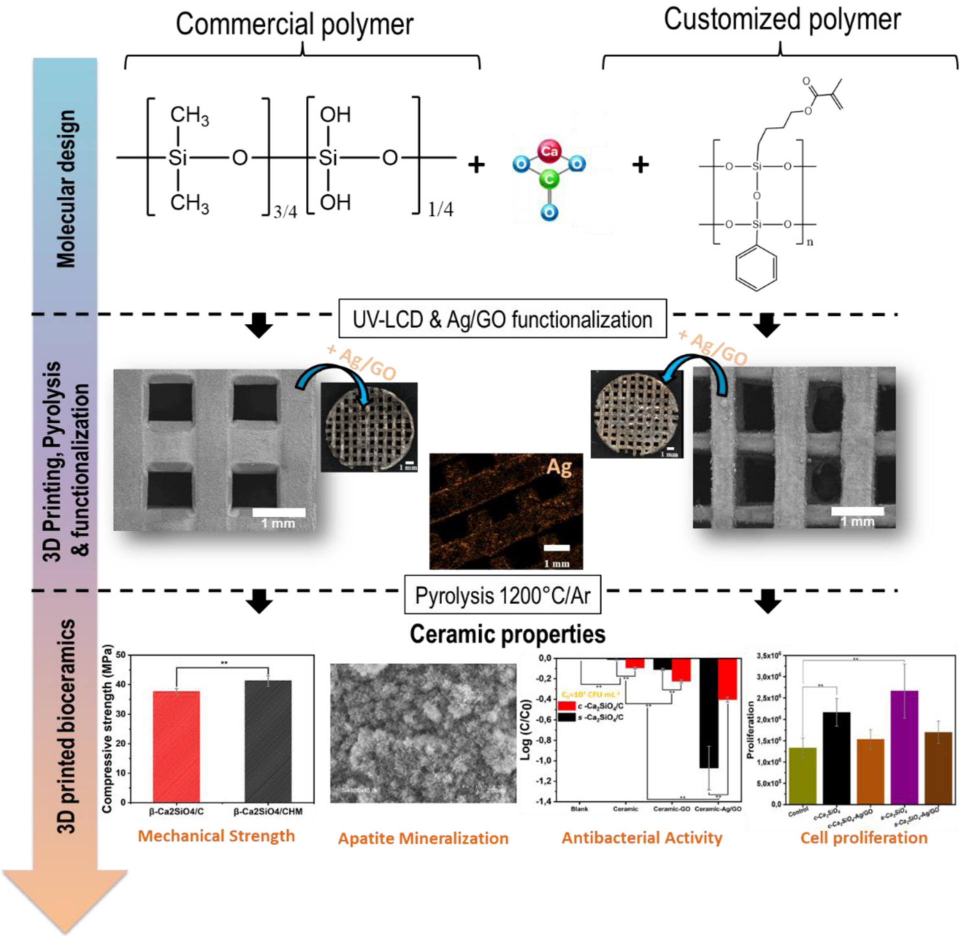

Fig. 1 Schematic diagram showing all the steps involved in the development of 3D bioceramic scaffolds, from molecular design to 3D printing and functionalization.

2530-85-0) and (trimethoxyphenylsilane, 98%, Sigma Aldrich France, CAS Number: 2996-92-1) used are named MOPTMS and PTMS respectively. Tetrahydrofuran (THF, anhydrous, >99.9%, Sigma Aldrich France, CAS Number: 109-99-9), dichlomethane (anhydrous, ≥99.8%, Sigma Aldrich France, CAS Number: 75-09-2), and magnesium sulfate ($MgSO_4$, anhydrous, ReagentPlus®, ≥99.5%, Sigma Aldrich France, CAS Number: 7487-88-9) were used without further purification. Potassium carbonate (K_2CO_3, anhydrous, >99%, Sigma Aldrich France, CAS Number: 584-08-7) was dried overnight under vacuum at 40 °C.

For the synthesis of graphene oxide nanosheets, potassium permanganate ($KMNO_4$, 99.0%, Alfa Aesar Germany, CAS Number: 7722-64-7), hydrogen peroxide (H_2O_2, ACS, 29–32% aqueous solution, Alfa Aesar Germany, CAS Number: 7722-84-1) and sulfuric acid (H_2SO_4, ACS reagent 95–98%, Sigma Aldrich France, CAS Number: 7664-93-9) were used as received without further purification.

For the synthesis of Ag/GO nanocomposite, sodium chloride (NaCl, crystalline powder PDV, ACS, 99.0%, Alfa Aesar Germany, CAS Number: 7647-14-5), ammonia solution ($NH_3{\cdot}H_2O$ 28%, VWR chemicals France, CAS Number: 1336-21-6), Glucose ($C_6H_{12}O_6$, ACS reagent, Sigma Aldrich France, CAS Number: 50-99-7), silver nitrate ($AgNO_3$, ACS reagent, ≥99.0%, Sigma Aldrich France, CAS Number: 7761-88-8) were used as received without further purification.

For antibacterial tests, a non-pathogenic Gram-negative *E. coli* bacterium (K12 DSM 423, from DSMZ, Germany) was used. All chemicals used were obtained from Merck, France. A ready-to-use Lysogeny Broth (LB) Miller medium (25 g L^{-1}) was chosen as the culture medium. LB medium containing tryptone (10 g L^{-1}), yeast extract (5 g L^{-1}) and NaCl (10 g L^{-1}), was mixed with microbiological agar at 15 g L^{-1} to obtain nutrient LB agar. In the particular case of the elaborated materials, they were wrapped in an aluminum foil and incubated for 24 h at 100 °C to render them free of microorganisms.

The gas used for pyrolysis is argon (99.999%) and was purchased from Linde France.

2.2. Preparation of silicone resins

Prior to use, calcium carbonate powder was sieved through 450 mesh to obtain an average particle size ~38 μm for promoting a good dispersion of $CaCO_3$ in the solvent.

2.2.1. Preparation of commercial resin blends. Silres MK (commercial preceramic polymer) was completely dissolved in isopropanol (0.8 mL per g of Silres MK) and the sieved $CaCO_3$ was added to obtain a Ca : Si molar ratio of 2 : 1. The mixture was kept under magnetic stirring at room temperature for 1 h. Then the photosensitive PLA eSUN resin was added to obtain a Silres MK/$CaCO_3$: PLA esun resin mass ratio of 50 : 50. The mixture was kept under magnetic stirring at room temperature for 2 h, protected from light.

2.2.2. Preparation of "customized" resin. A (phenyl-*co*-methacryl)silsesquioxane resin which will be named "customized" resin throughout this work was synthesized by hydrolysis of a silane monomer followed by a condensation and polymerization step in the presence of potassium carbonate K_2CO_3 as catalyst in a H_2O/THF solvent mixture at room temperature according to the work of Choi *et al.*[66] In a 200 mL Schlenk flask, deionized water (2.4 g, 0.133 mol) and K_2CO_3 (0.02 g, 0.145 mmol) were stirred for 10 minutes. Then, THF (4 g, 0.056 mol) was added and stirring continued for 30 minutes. Finally, a mixture of 0.04 mol (3-(trimethoxysilyl)-propyl methacrylate) and (trimethoxyphenylsilane) (R_{molar} = 60/40) was slowly added through a funnel over 15 minutes and the reaction was kept under magnetic stirring at room temperature for 96 h. The mixture was then separated into two phases, a colorless phase at the top and a cloudy one at the bottom. The crude and viscous products (cloudy phase) were obtained by decantation of the colorless mixed solvent. They were dissolved in methylene chloride (30 mL) and extracted with deionized water (30 mL) for 2 h in a separator funnel. Subsequently, the deionized water was removed and the solution was dried overnight using $MgSO_4$. The solution was filtered to remove the anhydrous $MgSO_4$ and then evaporated at 40 °C. The final powders were obtained after vacuum drying at 40 °C. The resin is recovered in the form of a glass-like powder. The "customized" preceramic polymer was dissolved in toluene (6.7 mL per gram of "customized" preceramic polymer) and the sieved $CaCO_3$ was added to obtain a Ca/Si molar ratio of 2/1. The mixture was then kept under magnetic stirring at room temperature for 2 h, protected from light. The schematic chemical structures of the two preceramic polymers are presented in Fig. S1 (ESI†).

2.3. Preparation of 3D printed ceramic scaffolds by UV-LCD

In this work, Zortrax INKSPIRE® (3D printer UV-LCD, Zortrax S.A., Poland) was used to print commercial and "customized" resins. Rectangular models (15 × 15 × 4 mm^3) were printed layer by layer using the UV-LCD technique, and the angle between each layer was 90°. The 3D scaffold printing parameters were optimized for a base layer exposure time of 120 s, followed by a 60 s exposure time for printing each layer and finally a 5 s exposure time between UV irradiation of each layer. After printing, the scaffolds were washed with isopropanol to remove excess unpolymerized PLA esun resin and "customized" resin, then the scaffolds were introduced into a UV chamber for 60 minutes to polymerize excess photosensitive resins that has not been removed during the washing step. Finally, the 3D polymer scaffolds were directly heated in a graphite furnace (Gero model HTK8) under an inert atmosphere (argon) at 300 °C with a heating rate of 2 °C min^{-1} and maintained for 3 h, then heated to 1200 °C and held for 4 h at this temperature with a heating rate of 2 °C min^{-1}. After cooling to room temperature with a cooling rate of 2 °C min^{-1}, these sintered scaffolds were removed from the furnace and used for further experiments. During all heat treatments, the materials were loaded into the furnace, after which the furnace chamber was evacuated for 1 h, then filled with argon at a flow rate of 250 mL min^{-1} during processing. The ceramic scaffolds resulting from the commercial and "customized" resin mixtures will be named c-Ca_2SiO_4/C and s-Ca_2SiO_4/C respectively.

2.4. Preparation of silver nanoparticles (AgNPs) decorated graphene oxide (GO) nanocomposite (Ag/GO) by liquid chemical reduction

Ag/GO nanocomposites were synthesized by reducing Ag ions and forming nanospheres *in situ* on GO nanosheets in the presence of glucose as a green reducing agent[58–60,63,67,68] (Fig. S2, ESI†). The Ag/GO nanocomposite was designated with a mass ratio (Ag : GO = 1 : 1). This ratio was chosen based on the work of Zhang *et al.*[63] In the first step, GO was prepared according to modified Hummers' method from graphite powder[69] (Fig. S2, ESI†). In a typical synthesis, graphite is oxidized with concentrated sulfuric acid and potassium permanganate. Deionized water was slowly added, followed by hydrogen peroxide. GO was then washed with deionized water and centrifuged several times until a concentrated solution with neutral pH was obtained. The GO solution (1 g L^{-1}) was sonicated for 4 h prior to use. GO was decorated with AgNPs as follows: first, 1 mL of ammonia solution (28%) was added to 40 mL of H_2O to prepare a dilute ammonia solution. Then a glucose solution of 0.03 mol L^{-1}, an $AgNO_3$ solution of 0.6 mol L^{-1} and a NaCl solution of 0.01 mol L^{-1} were prepared for later use. Next, $Ag(NH_3)_2OH$ was prepared by adding the dilute ammonia solution to 3.09 mL of $AgNO_3$ solution until the precipitate disappeared. The resulting silver–ammonia solution was added to 40 mL of GO solution and heated to 60 °C for 30 minutes. Next, 10 mL of glucose solution was added to reduce $Ag(NH_3)_2OH$ for 1 h under magnetic stirring. Afterwards, 10 mL of NaCl solution was added to the resulting dispersion and the precipitate was washed three times with deionized water. Finally, the Ag/GO nanocomposite was protected from light and stored in a refrigerator.

2.5. Preparation of Ag/GO modified c-Ca_2SiO_4/C and s-Ca_2SiO_4/C scaffolds

To prepare Ag-modified c-Ca_2SiO_4/C and s-Ca_2SiO_4/C scaffolds, 1 : 1 Ag/GO nanocomposites were sonicated for 1 h to form a homogeneous suspension of Ag/GO in deionized water. Then, 4 mL of the suspension was added to a beaker and the suspension diluted to 20 mL. Groups of 8 scaffolds of each ceramic type were immersed in the Ag/GO solution (20 mL) using a dip coater (Ossila) according to the following optimized program: immersion speed: 10 mm s^{-1}, immersion time: 10 min, withdrawal speed: 20 mm s^{-1}, drying time: 5 min and then dried for 30 min in an oven at 120 °C. The cycle was repeated 5 times for each scaffold to adjust the Ag/GO content.

2.6. Antibacterial activity of Ag/GO modified c-Ca_2SiO_4/C and s-Ca_2SiO_4/C scaffolds

2.6.1. Bacterial growth. Cultures were made from frozen aliquots of *E. coli* stored at −20 °C in 20% v/v glycerol. Aliquots were rehydrated in LB medium and sub-cultured in LB medium (at 4% v/v). Bacterial cultures were grown in Erlenmeyer flasks closed with breathable caps (to ensure sterility and continuous air entry). The flasks were incubated on a rotary shaker (30 °C and 110 rpm) overnight until the stationary phase was reached. To control the culture prior to its use for antimicrobial tests, a sample (1 mL) of the culture was sterilely collected and its optical density at 600 nm (OD_{600}) was measured. Optical density was correlated with bacterial concentration in CFU mL^{-1} (CFU standing for colony-forming units, *i.e.*, the number of bacteria).[70]

2.6.2. Antibacterial activity of scaffolds modified by Ag/GO functionalization. A liquid assay was implemented to assess the bactericidal ability of the different scaffolds (Fig. S3, ESI†). The culture was centrifuged (for 12 minutes at 4000 rpm, 12 °C) to separate the cells from the medium. The recovered *E. coli* pellets were then resuspended in phosphate buffer (PBS, pH = 7.0 ± 0.1) exempt from nutrients to avoid bacterial growth. The bacterial suspension obtained was then diluted in PBS to reach a concentration of $1.8 \pm 0.8 \times 10^7$ or $1.1 \pm 0.0 \times 10^4$ CFU mL^{-1}. The resulting bacterial suspension was dispensed into 25 mL glass vials closed with a breathable cap (5 mL per vial) and containing the different types of scaffolds that were prior sterilized at 100 °C overnight. The vials were then incubated for bacterial counting on a rotary shaker (30 °C and 160 rpm) for 3 h. Initial and final bacteria concentrations were measured. All experiments were duplicated. As control reactors, bacteria without scaffolds were used.

Bacterial concentrations (C, CFU mL^{-1}) were measured by the conventional plate assay method. Liquid samples were diluted by tenfold and each dilution (200 μL) was spread onto LB agar plates, along with the undiluted sample (200 μL). All plates were then incubated for 24 h at 37 °C to allow colonies to grow, and colonies were counted on the plates with the appropriate dilution. Bacterial concentrations C in the samples were calculated as the average number of colonies divided by the inoculated volume, taking into account the sample dilution factor. The limit of quantification was 5 CFU mL^{-1}. Antibacterial activity was characterized by calculating the associated log removal value. The log removal value was defined as the logarithm to base 10 of the ratio between the bacterial concentration C measured after 3 h of treatment and the initial concentration C_0. The more negative this ratio, the greater the removal caused by the material. In the case of total removal, the log removal value has been set at $-\log(C_0)$.

Tests were also carried out to determine whether silver was released from Ag/GO-modified scaffolds, and whether this silver could have an antibacterial action. To do this, the scaffolds were first incubated in PBS (5 mL per vial) on a rotary shaker (30 °C and 160 rpm) for 3 h, then the materials were removed from the PBS. The bacterial suspension was then added to the PBS solution obtained after contacting the material; 50 μL of the most concentrated bacterial suspension (*i.e.* 10^9 CFU mL^{-1}) was added to reach a bacterial concentration of 1.8×10^7 CFU mL^{-1} after mixing, while avoiding significant dilution of desorbed silver. The mixture was incubated for 3 h on a rotary shaker (30 °C and 160 rpm). Bacterial concentrations were measured at the beginning and end of incubation as described above.

2.7. Degradation and apatite mineralization ability of scaffolds

The c-Ca_2SiO_4/C and s-Ca_2SiO_4/C ceramic scaffolds were incubated in freshly made SBF simulated body fluid at a ratio of

10 mg scaffold per 7 mL SBF in a rotary shaker (37 °C, 70 rpm) for a period of 28 days. SBF was prepared to reproduce the ionic concentration of human blood plasma according to the standard procedure developed by Kukubo *et al.*[71] The pH value of the SBF solution and the weight of dried scaffolds were recorded by changing SBF every 48 h. The tests were repeated twice to validate the results.

2.8. Cell proliferation and cytotoxicity

2.8.1. *In vitro* cell culture. Bone marrow-derived mesenchymal stem cells (BM-MSCs) were obtained from ATCC (American Type Culture Collection, Spain) and were used to assess the biocompatibility of the samples tested. Cells were cultured according to standard cell culture protocol using complete DMEM culture medium, consisting of 10% fetal bovine serum (FBS) and 1% antibiotic (penicillin and streptomycin P/S) in a 5% CO_2 incubator at 37 °C. When the cells had reached a confluence level around 70–80%, the medium was removed, the cells were washed gently with PBS to remove the remaining medium and trypsinization was performed using 0.25% trypsin–EDTA. Detached cells were centrifuged at 1500*g* for 5 min and the cell pellet was redistributed with fresh medium for cell passage. Every time, the cell number was counted by using an automated Invitrogen cell counter (Invitrogen, Carlsbad, CA, USA).

2.8.2. Cell proliferation. Prior to cell culture, all samples tested were UV sterilized for 45 minutes by using a UV Sterilizer, 9 W, 60 Hz (SKU: OT-HSYXF-2624-EU, model YM-9002, China). Sterilized samples were transferred to 48-well culture plates and BM-MSCs with a cell density of 1×10^4 were seeded on top of the samples. Cells without samples were considered the control. The cells were allowed to grow for 7 days and the total number of cultured cells was counted by an automated cell counter (Invitrogen), after trypsinizing the cells with 0.25% trypsin-EDTA following the standard protocol. The percentage of cell proliferation in tested samples was calculated by comparison with the control group.

2.8.3. Cell cytotoxicity. The cytotoxic effect of the bioceramics was determined by the MTT Assay Protocol according to a previously established protocol.[72] Briefly, BM-MSCs were seeded on top of the samples at a density of 1×10^4 cells in 48-well culture plates as previously described, and positive control cells were seeded without bioceramics. The MSCs with bioceramics were cultured for 7 days before being treated with MTT. To this end, MTT reagent was prepared with a concentration of 5 mg in 1 mL PBS and 50 μL of MTT reagent was added to each well with the culture medium for 2 h. Then, the cells were briefly washed with PBS twice and formazan crystals were solubilized with DMSO at 37 °C, 5% CO_2 for 15 minutes. Then 100 μL were transferred to a 96-well plate with a transparent flat bottom, and the absorbance was recorded at 570 nm in a SpectraMAX Id3 plate reader.

2.8.4. Statistical analysis. Significant differences ($p < 0.05$) between each test were obtained by using one-way analysis of variance (ANOVA). All experiments presented in this study were carried out in triplicate and results were expressed as a mean ± standard deviation.

2.9. Characterization

2.9.1. Physical and chemical properties. The two preceramic polymers (commercial Sirles MK and "customized"), graphene oxide and Ag/GO nanocomposite were characterized by Fourier Transform Infrared (FTIR) (Nicolet 370 FTIR spectrometer using an ATR system), X-ray diffraction (PANALytical Xpert-PRO with Cu radiation at 0.154, Easton, PA, USA), $200 < \lambda < 600$ nm, external calibration method, X-ray diffraction (PANALytical Xpert-PRO with Cu radiation at 0.154 nm).

"Customized" polymer structure was investigated by ^{13}C and ^{29}Si solid-state NMR spectroscopy The spectra were recorded with a Bruker AVANCE 300 spectrometer (B_0 = 7.0 T, ν_0 (^1H) = 300.29 MHz, ν_0 (^{13}C) = 75.51 MHz, ν_0 (^{29}Si) = 59.66 MHz) using 4 mm Bruker probe at a spinning frequency of 12.5 kHz. ^{13}C CP MAS experiment was performed with ramped-amplitude cross-polarization (recycle delay = 3 s, CP contact time = 1 ms, optimized ^1H spinal-64 decoupling). Single pulse ^{29}Si MAS NMR spectra were recorded with a recycle delay of 60 s. Chemical shift values were referenced to tetramethylsilane for ^{13}C and ^{29}Si.

The Ag/GO nanocomposite was characterized by high-resolution transmission electron microscopy (HR-TEM, JEOL ARM 200 F, Japan) with an energy dispersive X-ray (EDX) analyzer and energy electron loss spectroscopy-EELS.

The chemical composition of c-Ca_2SiO_4/C and s-Ca_2SiO_4/C ceramics (before and after 7 days immersion in SBF) and Ag/GO functionalized ceramics were analyzed by energy dispersive X-ray spectroscopy (Detector: Oxford Instruments X-Max N SDD; Microscope: Zeiss EVO HD15). To detect the formation of the β-Ca_2SiO_4 phase and its purity, c-Ca_2SiO_4/C and s-Ca_2SiO_4/C ceramics were analyzed by X-ray diffraction (PANALytical Xpert-PRO with Cu radiation at 0.154 nm).

The graphene oxide GO and the Ag/GO nanocomposite were characterized using UV-Vis spectroscopy (Jasco V-570 UV-vis-NIR spectrophotometer Jasco Inc., Easton, PA, USA, $200 < \lambda < 600$ nm, and the external calibration method), Raman spectroscopy (inVia of Renishaw, with an Leica*50 objective) using a green excitation laser line (532 nm) and XPS photoelectron spectroscopy ESCALAB 250, ThermoElectron equipped with an Al Kα 1486.6 eV line as a monochromatic excitation source with a spot size of 400-μm. Samples for XPS were prepared on a gold-coated silicon wafer.

At the end of each bactericidal test, a quantitative analysis of total silver (soluble and particulate) desorbed from the functionalized ceramics materials (c-Ca_2SiO_4/C-Ag/GO; s-Ca_2SiO_4/C-Ag/GO) was performed. For these analyses, each liquid sample was diluted ten times in deionized water and acidified with 2.5% HNO_3 to completely solubilize the silver. Then, the samples were analyzed by atomic absorption spectrometry (Perkin-Elmer). The results were expressed in mg L^{-1}.

To determine the concentration of silver retained on the surface of c-Ca_2SiO_4/C and s-Ca_2SiO_4/C scaffolds, the materials were washed with 10 mL of an aqua regia solution (mixture of hydrochloric acid/nitric acid, in a 3 : 1 volume ratio) for 24 h, then diluted tenfold and filtered (0.2 mm Millipore cellulose acetate). Samples were then measured by Agilent 7700x

Quadrupole Inductively Coupled Plasma Mass Spectroscopy (ICP-MS).

2.9.2. Thermal analysis. To study the polymer-to-ceramic conversion, commercial Silres MK and ''customized'' preceramic polymers as well as additives ($CaCO_3$ and PLA esun resin) and finally mixtures of all c-Ca_2SiO_4/C and s-Ca_2SiO_4/C ceramic precursors were characterized by thermogravimetric analysis on a TGA-STD Q600 thermal analysis device under atmospheric pressure and nitrogen atmosphere from RT up to 1000 °C with a heating rate of 10 °C min^{-1}.

2.9.3. Mechanical properties. The compressive strength of the scaffolds was tested using a static materials testing machine (2.5 kN) (Zwick Roell, Ulm,Germany) at a crosshead speed of 0.01 mm s^{-1} (data from three or more trials).

2.9.4. Morphogical properties. The morphology of c-Ca_2SiO_4/C and s-Ca_2SiO_4/C ceramic scaffolds (before and after 7 days of immersion in SBF) was characterized by Scanning Electron Microscopy (Hitachi S4800, operating with an acceleration voltage between 0.1 kV and 30 kV). The morphology and structural properties were examined using high-resolution transmission electron microscopy (HR-TEM) (JEOL ARM 200F) with an attached EDX analyzer, operating at 200 kV. In addition, the morphology and surface roughness of Ag/GO functionalized scaffolds *i.e.* c-Ca_2SiO_4/C-Ag/GO and s-Ca_2SiO_4/C-Ag/GO were characterized using a super depth field three-dimensional microscope (VHX-1700, KEYENCE, Japan).

The porosity and density of the c-Ca_2SiO_4/C and s-Ca_2SiO_4/C scaffolds were measured using Archimedes' principle and water was used as a liquid medium. Porosity (P) was calculated according to the following formulation: $P = (W_{\mathrm{sat}} - W_{\mathrm{dry}})/(W_{\mathrm{sat}} - W_{\mathrm{sus}}) \times 100\%$, and density was calculated according to the formula: $\rho = W_{\mathrm{dry}} \times (\rho_{\mathrm{water}} - \rho_{\mathrm{air}})/(W_{\mathrm{dry}} - W_{\mathrm{sat}}) + \rho_{\mathrm{air}}$, where W_{dry} is the dry weight of the scaffolds, W_{sus} is the weight of the scaffolds suspended in water, W_{sat} is the weight of the scaffolds saturated with water, ρ_{water} is the density of water (1.0 g cm^{-3}), and ρ_{air} is the density of air (0.0012 g cm^{-3}).

2.10. Statistical analysis

For every quantitative characterization method, the Student test was used to evaluate if the data from every group of samples showed a significant difference ($^{**}p < 0.05$ for significant and $^{***}p < 0.005$ for highly significant statistical difference).

3. Results

3.1. Characterization of commercial Silres MK and ''customized'' preceramic polymers

Both Silres MK and ''customized'' preceramic polymers used as SiOC precursors were characterized by X-ray diffraction (XRD) and FTIR spectroscopy (Fig. S4, ESI†) to investigate their structure. In both cases, two diffraction peaks characteristic of the polysilsesquioxane ladder structure are observed[73] (Fig. S4(a), ESI†). The first sharp peak at 2θ 10.32° and 6.53° for Silres MK and ''customized'' preceramic polymers respectively derives from the periodic intramolecular chain-to-chain distance in the polysilsesquioxane structures. The second relatively large peak in both cases appears at 2θ 22.2° (d = 3.99 Å) and 19.53° (d = 4.53 Å) for Silres MK and ''customized'' preceramic polymers, respectively. This peak reveals the average thickness of the polysilsesquioxane structure. The thickness of the polysilsesquioxane structure of the ''customized'' polymer is greater than that of Silres MK. This is due to the presence of methacryl functions, which are longer and bulkier than the methyl functions of Silres MK polymer.

FTIR spectroscopy was used to determine more precisely the chemical structure of the two preceramic polymers (Fig. S4(b), ESI†). According to the general chemical formulation (Fig. S1, ESI†), the Silres MK and ''customized'' preceramic polymers show the absorption bands of different chemical functions. Indeed, the peaks ranging from 1000 to 1200 cm^{-1} (*i.e.* 1018.23 and 1101.15 cm^{-1}, 1018.24 and 1108.81 cm^{-1} respectively) for Silres MK and ''customized'' preceramic polymers result from the stretching vibration of Si–O–Si bond in the horizontal and vertical direction of the polysilsesquioxane structure. In the case of the Silres MK, absorption bands attributed to Si–CH_3 (762.22 cm^{-1}), Si–OH (863.95 cm^{-1}) and Si–CH (1271.34 cm^{-1}) bonds were detected. For the ''customized'' preceramic polymer, stretching vibrations of the C═C bond and the C═O carbonyl were clearly observed at 1635.36 and 1720.25 cm^{-1} respectively. This proves that the desired structure has been successfully synthesized by introducing the methacrylate functions directly onto the main chain, which will react with UV light during the stereolithography process. The ^{13}C CP MAS NMR spectrum (Fig. S5(a), ESI†) features peaks that can be attributed to C═C (methacrylate groups), C═C (phenyl groups) and methacryloxypropyl bonds. These results indicate that the trimethoxysilane monomers have been completely hydrolyzed and polymerized by condensation reaction to give the ''customized'' polymer. The ^{29}Si MAS NMR spectrum (Fig. S5(b), ESI†) of this polymer shows two peaks at −68 and −80 ppm, corresponding to propyl methacrylate-SiO_3 and phenyl-SiO_3 environments, respectively.

3.2. Characterization of preceramic polymer mixtures and c-Ca_2SiO_4/C and s-Ca_2SiO_4/C scaffolds

The study of polymer-to-ceramic conversion was carried out by TGA analysis under N_2 atmosphere. Fig. 2(a) and (b) show the TGA curves for all components of preceramic polymer mixtures with additives prior to printing (a) commercial and Silres MK and (b) ''customized''. In the case of Silres MK preceramic polymer with $CaCO_3$ and PLA esun resin, the TGA curve of PLA shows a significant weight loss from 400 °C and ends completely at 600 °C with a yield of 4.16%. This shows that the resin is completely organic and its role was solely to enable 3D printing of the scaffold. Moreover, the TGA curve for Silres MK shows a first weight loss around 230 °C due to cross-linking reactions. At temperatures above 350 °C, a second weight loss is observed due to decomposition and transformation reactions of the polymer into SiOC ceramic, with a ceramic yield of 83%. Calcium carbonate shows only one decomposition around 600 °C, corresponding to the formation of CaO with a yield of

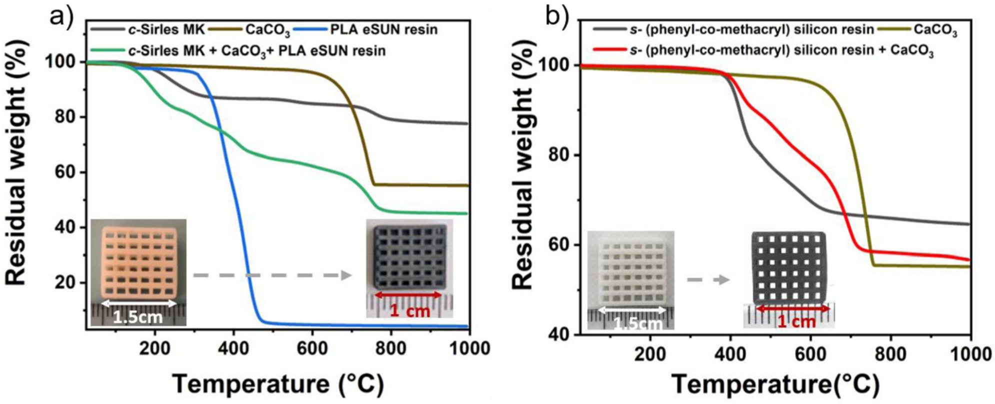

Fig. 2 TGA curves for all components of preceramic polymers with printing additives, (a) Commercial Silres MK and (b) "customized". Photographs of the c-Ca_2SiO_4/C and s-Ca_2SiO_4/C scaffolds before and after pyrolysis respectively in inset.

55.5%. Then, from 800 °C, SiOC and CaO react together to form β-Ca_2SiO_4 ceramic with an amorphous carbon phase coming from SiOC. The mixture of Silres MK, $CaCO_3$ and PLA resin shows several decomposition stages, the first starting at 180 °C due to solvent removal and cross-linking reactions. Conversely, TGA analysis of the "customized" preceramic polymer (Fig. 2(b)) shows good thermal stability The second decomposition of the PLA resin and conversion of the polymer into ceramic occurs between 200 and 480 °C with a ceramic yield of 55%, corresponding to the weight loss (58%), with a ceramic yield of 65% at 800 °C. It should be noted that even the methacrylic fractions were stable up to 400 °C. The decomposition of the polymer occurs between 400 and 800 °C by release of dihydrogen according to dehydrocoupling reactions. This thermal stability can be attributed to the structural strength as well as the compact, closed structure of the polysilsesquioxane polymer. At 800 °C too, SiOC and CaO react together to produce the desired ceramic. In contrast, the mixture of the "customized" polymer and $CaCO_3$ shows two decompositions, one around 400 °C (conversion of polymer to ceramic) and the other around 600 °C, corresponding to the decomposition of $CaCO_3$ to CaO. From 800 °C, we have stability up to 1000 °C, indicating the chemical reaction that will lead to ceramic formation. We obtained a ceramic yield of 56%, corresponding to a scaffold mass loss after pyrolysis of ~58%.

The scaffolds, initially printed with a rectangular structure measuring 15 × 15 × 4 mm^3, appear white due to the inclusion of $CaCO_3$ as an active filler. This filler will later undergo a reaction during heat treatment to produce the desired ceramic material. The pyrolysis process is pivotal as it transforms the polymers into ceramics. Following pyrolysis, the scaffolds undergo volume shrinkage relative to their initial green state (measuring 10 × 10 × 2 mm^3). This shrinkage is attributed to the decomposition of organic moieties during pyrolysis. Consequently, the black coloration arises from the formation of free carbon rich SiOC as a result of the conversion of preceramic polymers into ceramics.

Fig. 3(a) and (b) show the surface morphologies of c-Ca_2SiO_4/C and s-Ca_2SiO_4/C ceramic scaffolds after pyrolysis at 1200 °C under argon atmosphere. Both types of scaffold retain their shape and structure of interconnected, parallel and regular macropores (*ca.* 800 μm). The distance between the spacers is about 821 μm and 800 μm, corresponding to a volume shrinkage relative to the initial scaffolds before pyrolysis of approximatively 15.62% and 17.78% for c-Ca_2SiO_4/C and s-Ca_2SiO_4/C, respectively. On the other hand, the surface of s-Ca_2SiO_4/C scaffold exhibits a greater roughness compared to that of c-Ca_2SiO_4/C. In addition, pores with diameters between 10 and 80 nm can be observed in the walls, formed as a result of the decomposition of low molecular weight species during pyrolysis. The surface composition of these scaffolds was observed by EDX as shown in Fig. 3(c) for c-Ca_2SiO_4/C and in Fig. 3(d) for s-Ca_2SiO_4/C. EDX mappings show a homogeneous distribution of all elements (Ca, Si, O) in β-Ca_2SiO_4 ceramic scaffolds. In addition, carbon is present and homogeneously dispersed on the surface of the scaffolds. This carbon phase (Si–C and amorphous carbon) results from the decomposition of the preceramic resins during pyrolysis, which will then react with the CaO resulting from the decomposition of $CaCO_3$ to finally generate the β-Ca_2SiO_4/Carbon ceramic.

Fig. S6 (ESI†) shows the X-ray diffraction peaks of the c-Ca_2SiO_4/C and s-Ca_2SiO_4/C scaffolds. In both cases, the peaks correspond to the diffraction peaks of the β-Ca_2SiO_4 phase (JCPDS map 33-0302). This indicates the formation of the desired ceramic phase without impurities and confirms the successful conversion of the preceramic polymer to ceramic.

The scaffold porosity measures 70 ± 1.5% and 59.8 ± 0.7% for c-Ca_2SiO_4/C and s-Ca_2SiO_4/C respectively, as shown in Fig. 4(a). These results are consistent with the compressive strength measurements, which indicate values of 37.6 ± 1.05 MPa and 41.25 ± 1.76 MPa for c-Ca_2SiO_4/C and s-Ca_2SiO_4/C respectively (Fig. 4(b)). It can therefore be concluded that the ceramic made from the "customized" preceramic polymer exhibits superior mechanical strength compared to that made from the commercial preceramic polymer Silres MK.

3.3. Characterization of Ag/GO nanocomposite

Silver (Ag) is widely recognized for its potent antibacterial properties, making it a valuable material for treating wounds

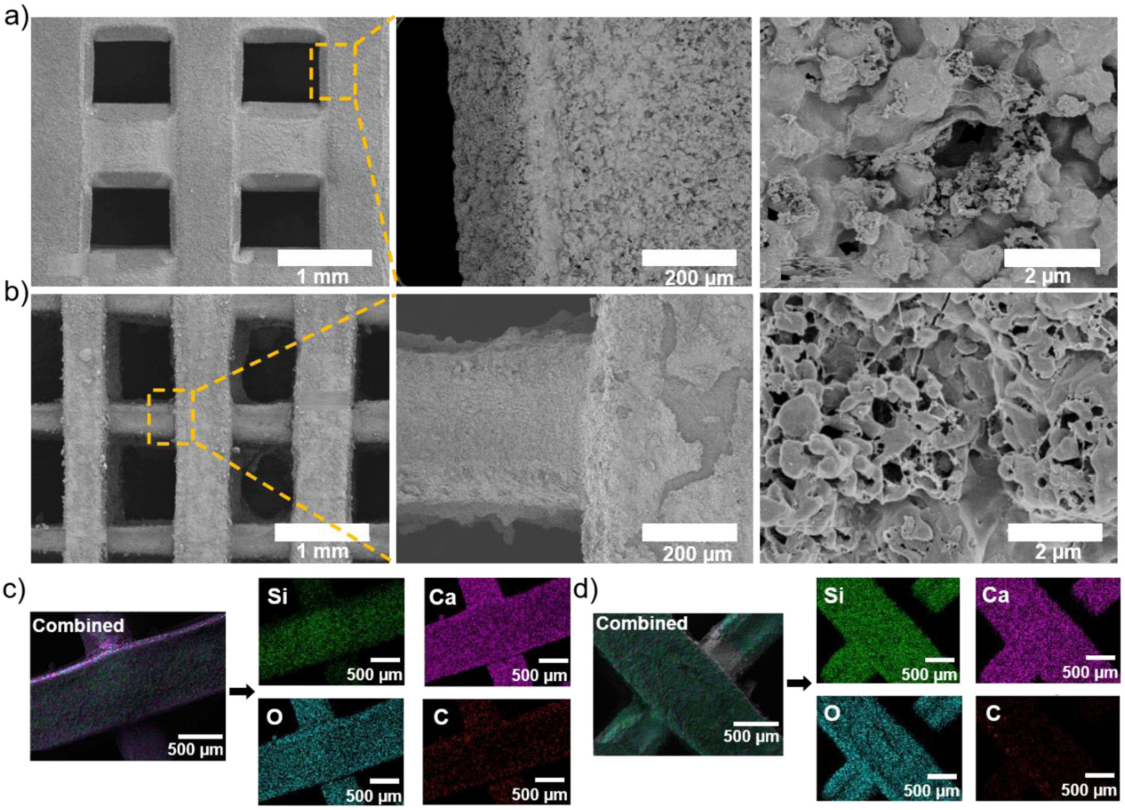

Fig. 3 Morphological and compositional characterization of c-Ca_2SiO_4/C and s-Ca_2SiO_4/C scaffolds after pyrolysis at 1200 °C. SEM images of (a) c-Ca_2SiO_4/C and (b) and s-Ca_2SiO_4/C scaffolds. Element mapping (EDX) of the surface of (c) c-Ca_2SiO_4/C and (d) s-Ca_2SiO_4/C scaffolds.

and various chronic diseases linked with bacterial infections.[53,74–79] Nevertheless, the direct use of metallic silver often leads to the rapid release of silver ions, thereby restricting its biomedical applications.[80] Conversely, these limitations can be addressed by immobilizing Ag^+ ions onto a 2D support such as graphene oxide (GO), where they can undergo reduction to stable Ag^0 over time, offering a more controlled and sustained antibacterial effect.

Fig. 5(a) shows the ultraviolet-visible (UV-vis) light absorption spectra of the aqueous dispersions of GO and Ag/GO. GO shows two characteristic absorption peaks with a maximum at 254.5 nm and a shoulder at 302 nm, corresponding respectively to the π–π^* transitions of the aromatic C–C bond and the n–π^* transitions of the C═O bond in graphene oxide.[81–83] The peak at 254.5 nm is shifted to 277.5 nm after the thermal reduction treatment, which resulted in low GO reduction.[84] The incorporation

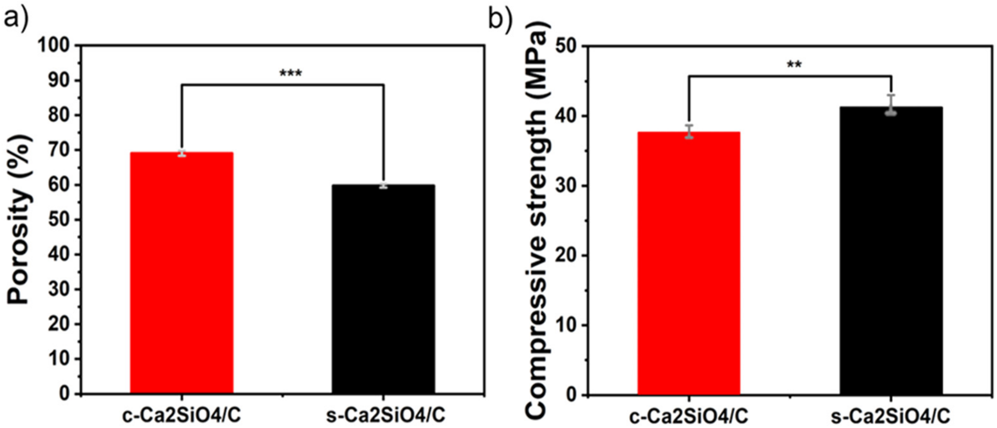

Fig. 4 (a) Porosity and (b) compressive strength of c-Ca_2SiO_4/C and s-Ca_2SiO_4/C scaffolds. **($p < 0.05$) or ***($p < 0.005$) indicate significant difference.

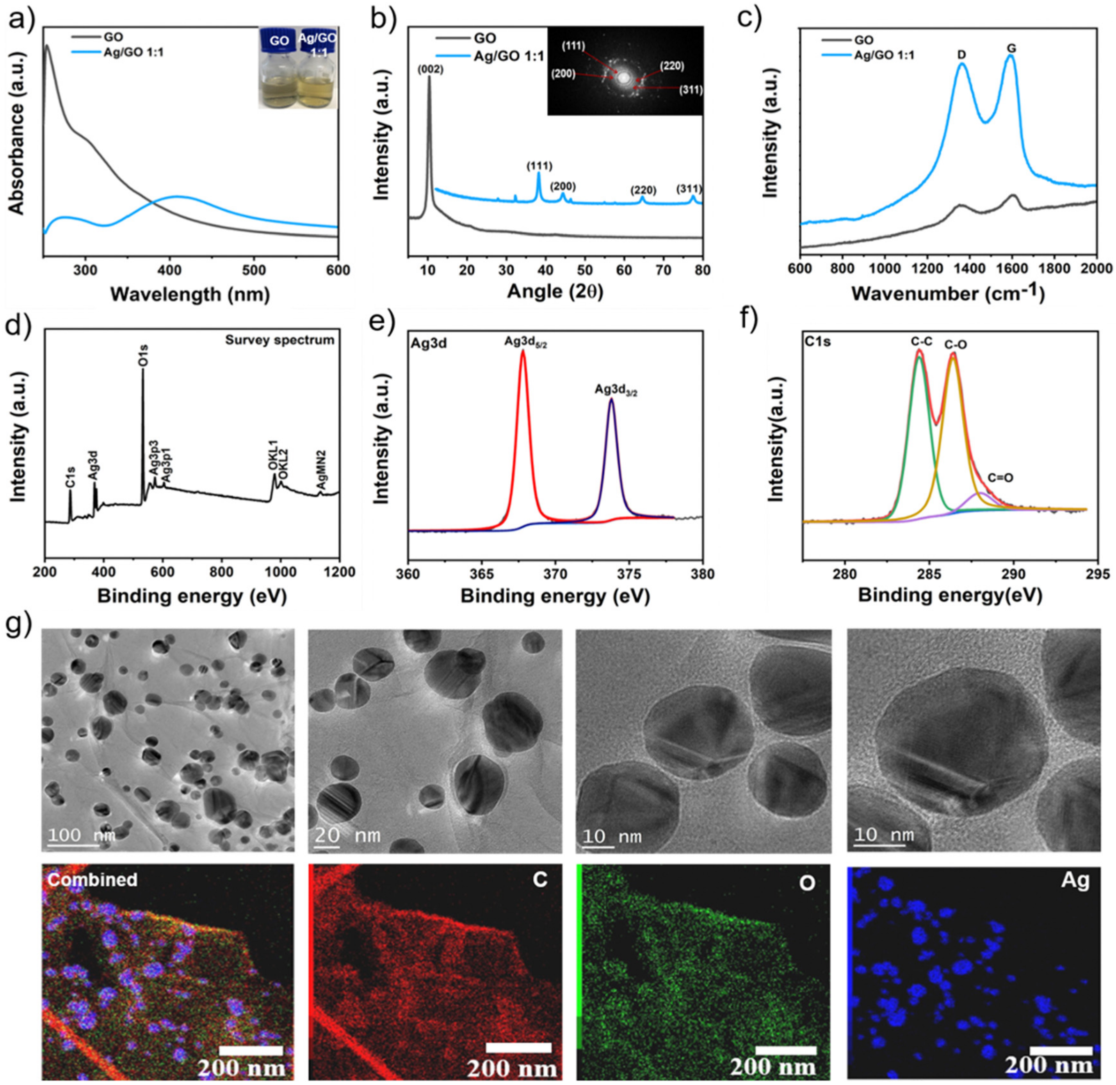

Fig. 5 (a) UV-vis absorption spectra of the aqueous dispersion of GO and Ag/GO insets: optical images of GO and Ag/GO 1 : 1 (50 μg mL^{-1}), (b) XRD patterns of GO and Ag/GO and SAED patterns, (c) Raman spectra of GO and Ag/GO excited with a green laser line (532 nm), (d) XPS survey spectra of Ag/GO, (e and f) high-resolution XPS spectra of Ag3d and C1s of Ag/GO, (g) TEM images of Ag/GO and EDX mapping.

of Ag on GO nanosheets leads to an absorption peak at 411 nm which is attributed to the surface plasmon resonance of colloidal silver, indicating that Ag nanoparticles have been deposited on GO sheets.[85]

Fig. 5(b) shows the X-ray diffraction (XRD) patterns of the GO samples and the Ag/GO composite. GO shows a typical diffraction peak at 10.16°, corresponding to the (002) diffraction peak of graphene oxide. The formation of AgNPs was confirmed through the presence of diffraction patterns of the silver crystal structure, corresponding to the standard diffraction (XRD) pattern (JCPDS no. 04-0783). The four diffraction peaks located at 2θ 38.1°, 44.3°, 64.5° and 77.5° represent the (111), (200), (220) and (311) crystallographic planes respectively for the face-centered cubic structure of crystalline silver and the selected area electron diffraction (SAED) pattern.[86–88] The crystallite size of Ag nanoparticles supported on GO was determined from XRD using the Scherrer equation, yielding a size of 30.02 ± 3.85 nm, consistent with observations from TEM images. Furthermore, the disappearance of the typical peak at 2θ = 10.16° of GO after functionalization with AgNPs suggests that the silver nanoparticles hinder the re-stacking of graphene sheets.[85]

The Raman spectrum of GO (Fig. 5(c)) shows two prominent peaks, the D-band (1363.35 cm^{-1}) and the G-band (1590.171 cm^{-1}), which are attributed to the in-plane vibrations of aromatic carbon atoms in the graphitic structure, but also the mode of the κ-point phonons of the A_{1g} symmetry and the E_{2g} phonon of the sp^2 C atoms, respectively (I_D/I_G = 0.85). In addition, the maximum intensity of Ag/GO is higher than that of GO with a similar I_D/I_G ratio (= 0.961), which is due to surface-enhanced Raman scattering (SERS) of the intense local electromagnetic fields of Ag nanoparticles accompanying plasmon resonance.[89]

Fig. 5(d) shows the X-ray photoelectron survey spectra (XPS) of the Ag/GO composite. The GO shows only XPS peaks of C1s and O1s, while the Ag/GO composite shows the signals of Ag3d, $Ag3p_1$, $Ag3p_3$ and Ag MN2.[90] The relevant high-resolution Ag3d XPS spectrum (Fig. 5(e)) shows the existence of two binding energies for Ag 3d for the Ag/GO sample, 367.8 and 373.8 eV, with a difference of 6.0 eV corresponding to $Ag3d_{5/2}$ and $Ag3d_{3/2}$, respectively. This proves the formation of metallic silver particles. The standard binding energies of pure metallic silver are 368.1 and 374.1, the shift to the lower binding energy may be due to the electron transfer between silver nanoparticles and graphene oxide.[83] The XPS C1s spectrum of GO (Fig. 5(f)) indicates the presence of all the functional groups initially present in the graphene oxide (epoxy, hydroxy and carboxyl) with relatively high intensity. This allows us to conclude that the addition of small amount of glucose resulted in a very small reduction in GO after the *in situ* chemical reduction. This also provides a measurement of the hydrophilicity degree of the Ag/GO composite. This hydrophilicity will subsequently allow the formation of hydrogen bonds between the oxygenated groups present on the Ag/GO sheets and the proteins of the cell membranes, which facilitates the direct contact of the Ag/GO sheets with the bacteria. The wrapping of Ag/GO sheets around microbial cells can eventually block the cells' access to nutrients and cause cell death.[85]

Transmission electron microscopy (TEM) images of the Ag/GO composite (Fig. 5(g)) reveal the spherical shape of the AgNPs with an average size of 30 ± 7.85 nm, and show that AgNPs are attached randomly, homogeneously and densely to the graphene surface. EELS observations of the Ag/GO composite confirm that AgNPs are present on the surface of transparent graphene nanosheets (extremely thin) (see the blue dots).

3.4. Characterization of Ag/GO modified c-Ca_2SiO_4/C and s-Ca_2SiO_4/C scaffolds

Fig. 6(a) and (c) show the morphology of c-Ca_2SiO_4/C and s-Ca_2SiO_4/C scaffolds, a_1; c_1 after 3D printing, a_2; c_2 after pyrolysis under argon at 1200 °C and a_3; c_3 after dip coating with Ag/GO respectively. Photos a_1 and c_1 show the rectangular grid-like scaffold of ($15 \times 15 \times 4$ mm^3) after 3D printing by UV-LCD of preceramic polymers with the additives, in which the white color is due to the presence of calcium carbonate in large quantities. Photos a_2 andc_2 show the ceramic scaffold after pyrolysis at 1200 °C under argon. The pyrolysis step is essential to enable conversion of the preceramic polymers into ceramics, the black color is due to the formation of a homogeneous phase of amorphous carbon in β-Ca_2SiO_4 ceramic, as silicon-based preceramic polymers generate SiOC during the thermal treatment at high temperature under inert atmosphere.[17,91,92] Photos a_3 and c_3 show the black ceramic scaffolds dip-coated with Ag/GO. Dip-coating was used to optimize the amount of silver deposited on the 3D ceramic scaffolds. This technique also enabled us to reproducibly fabricate scaffolds functionalized with Ag/GO in order to study their antibacterial activity. Finally, 3D microscopy images (Fig. 6(b) and (d)) of the c-Ca_2SiO_4/C and s-Ca_2SiO_4/C scaffolds modified with Ag/GO show the conservation of the 3D structure after pyrolysis and functionalization in both systems. However, in the case of the s-Ca_2SiO_4/C ceramic, the Ag/GO composite was homogeneously deposited on the scaffold surface, this is confirmed by the homogeneous color all over the surface of the scaffolds, contrarily to the c-Ca_2SiO_4/C scaffold where we can observe areas not homogeneously coated with Ag/GO. Moreover, we detected a reduction in the diameter (in both cases 50% volume shrinkage), pore size and thickness (55.25% and 44.35% volume shrinkage for c-Ca_2SiO_4/C and s-Ca_2SiO_4/C respectively) of the scaffolds.

3.5. Antibacterial activity of Ag/GO modified c-Ca_2SiO_4/C and s-Ca_2SiO_4/C scaffolds

Fig. 7 shows the *E. coli* removals obtained after 3 h of contact with the different scaffolds. Compared with the blank, the s-Ca_2SiO_4/C scaffold shows no antibacterial activity, while the c-Ca_2SiO_4/C scaffold shows a slight decrease in bacteria concentration (−0.1 log removal), which could be attributed to bacteria adsorption. The c-Ca_2SiO_4/C-GO and s-Ca_2SiO_4/C-GO scaffolds produced small but significant log removal values (respectively −0.2 and −0.1), which could be due to bacterial adsorption or the weak biocidal action of GO. The incorporation of Ag/GO nanoparticles on the scaffold surface (ceramic Ag/GO) induced a net elimination of *E. coli*: −0.4 ± 0.0 for c-Ca_2SiO_4/C-Ag/GO and −1.1 ± 0.2 for s-Ca_2SiO_4/C-Ag/GO. A log removal value of

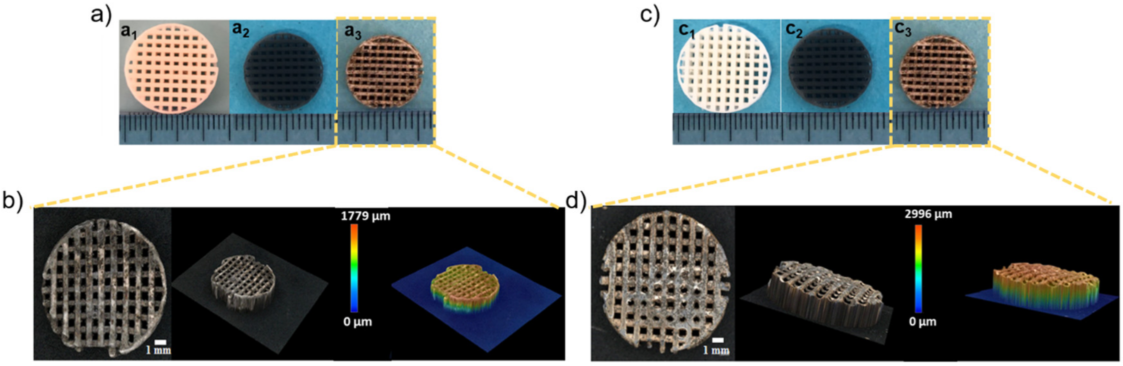

Fig. 6 (a) and (c) Photographs of c-Ca_2SiO_4/C and s-Ca_2SiO_4/C scaffolds, (a_1 and c_1) after 3D printing, (a_2 and c_2) after pyrolysis under argon at 1200 °C and (a_3 and c_3) after dip coating with Ag/GO; (b) and (d) 3D images of c-Ca_2SiO_4/C-Ag/GO and c-Ca_2SiO_4/C-Ag/GO scaffolds.

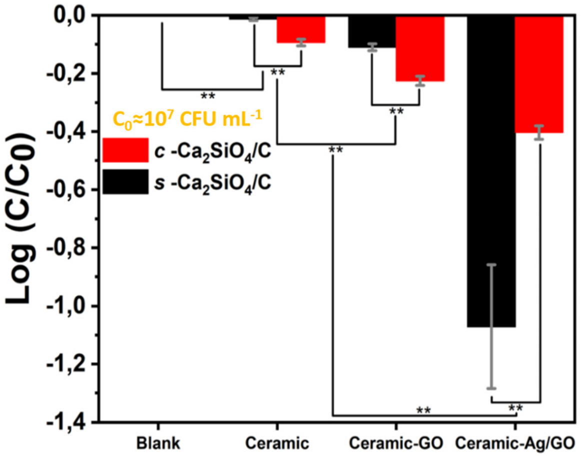

Fig. 7 Antibacterial activity against *E. coli* by scaffolds: ceramic; GO and Ag/GO functionalized ceramic scaffolds. C_0 is the initial bacterial concentration (1.8 ± 0.8 10^7 CFU mL^{-1}) and C (CFU mL^{-1}) the concentration of bacteria measured after 3 h incubation. **($p < 0.05$) indicates a significant difference between the different materials and conditions.

−1.0 means that the material removes 90% of the bacteria present in solution. The s-Ca_2SiO_4/C-Ag/GO therefore has significant antibacterial activity.

To determine the silver content deposited on the scaffolds' surfaces, ICP-MS analysis was conducted, revealing $0.03 \pm 6 \times 10^{-3}$ mg and 0.18 ± 0.01 mg of Ag fixed into c-Ca_2SiO_4/C-Ag/GO and s-Ca_2SiO_4/C-Ag/GO scaffolds, respectively. The high biocidal activity observed for the s-Ca_2SiO_4/C-Ag/GO scaffold can therefore be attributed to its higher silver content at the material's surface. This increased silver concentration potentially increases the frequency of bacterial encounters with the silver surface, consequently enhancing its antibacterial efficacy.

To better characterize material surfaces and the resulting interaction between grafted silver nanoparticles and bacteria, super depth field three-dimensional microscopy and energy dispersive spectrometry (EDX) analysis were implemented to observe the morphology, composition and surface roughness of the scaffolds. The results are shown in Fig. 8 and Fig. S7, S8 (ESI†).

EDX mapping reveals a clear difference between the s-Ca_2SiO_4/C-Ag/GO scaffold (Fig. 8(a)) and the c-Ca_2SiO_4/C-Ag/GO scaffold (Fig. 8(b)). In the former case, silver is uniformly dispersed over the entire surface, while in the latter, aggregates of silver nanoparticle are observed. The average atomic percentage of silver on the surface is 2.2 for s-Ca_2SiO_4/C-Ag/GO. In the case of c-Ca_2SiO_4/C-Ag/GO, an atomic percentage of 1.88 was measured for the homogeneously distributed silver portion, while an atomic percentage of 3.64 was observed for the silver nanoparticle aggregates. The non-homogeneous distribution of silver on the surface of c-Ca_2SiO_4/C-Ag/GO is likely attributed to the lower silver content deposited on the surface.

In addition, the s-Ca_2SiO_4/C-Ag/GO scaffold had a rougher surface than the c-Ca_2SiO_4/C-Ag/GO scaffold (Fig. 8(c) and (d)). Similarly, the s-Ca_2SiO_4/C-Ag/GO scaffolds exhibited higher R_a and R_z values (where R_a represents the arithmetic average rugosity of the surface and R_z indicates the maximal height of the surface); (Fig. 8(e)). It is widely recognized that an R_a roughness of several tens of microns increases the specific surface area available for bacterial interaction, thus facilitating contact with the surface.[93] The combination of increased roughness and higher silver content may therefore explain the superior biocidal activity observed in s-Ca_2SiO_4/C-Ag/GO as observed in Fig. 7.

To verify the desorption of silver from Ag/GO functionalized ceramics and its potential contribution to the antibacterial properties of the material, the ceramics were incubated in

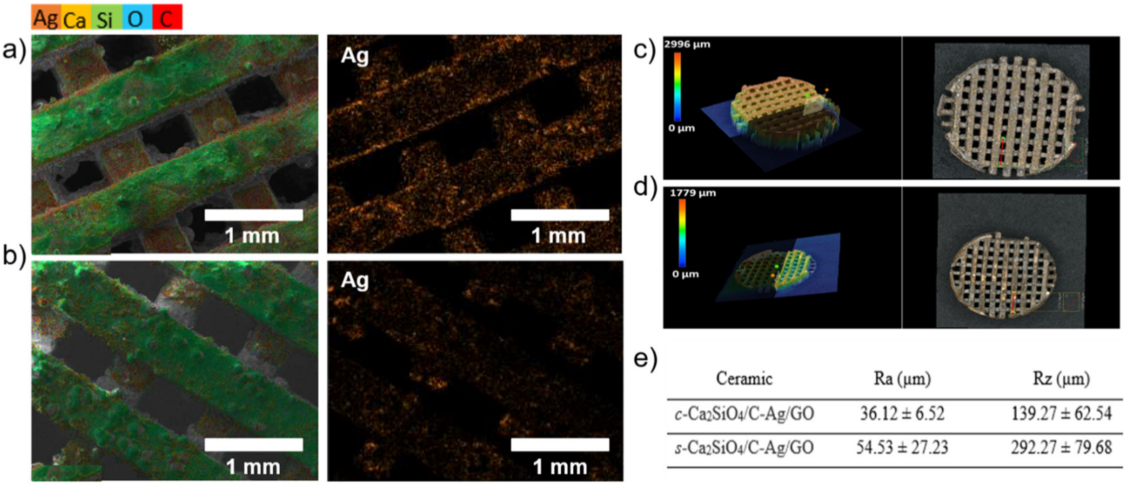

Ceramic	Ra (µm)	Rz (µm)
c-Ca_2SiO_4/C-Ag/GO	36.12 ± 6.52	139.27 ± 62.54
s-Ca_2SiO_4/C-Ag/GO	54.53 ± 27.23	292.27 ± 79.68

Fig. 8 Topographical and compositional characterization of c-Ca_2SiO_4/C and s-Ca_2SiO_4/C scaffolds functionalized with Ag/GO nanoparticles. Elemental mapping (EDX) of (a) s-Ca_2SiO_4/C-Ag/GO and (b) c-Ca_2SiO_4/C-Ag/GO scaffolds. 3D images of the surface roughness of (c) s-Ca_2SiO_4/C-Ag/GO and (d) c-Ca_2SiO_4/C-Ag/GO scaffolds. Surface roughness (e) of c-Ca_2SiO_4/C-Ag/GO and s-Ca_2SiO_4/C-Ag/GO scaffolds; R_a (µm) is the arithmetic average rugosity of the surface and R_z (µm) the maximal height of the surface.

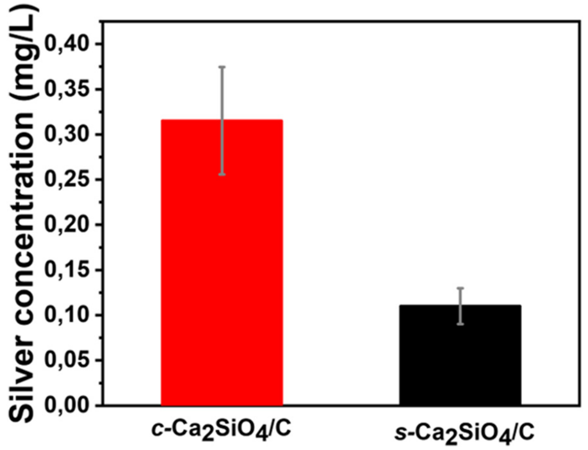

Fig. 9 Concentrations of silver desorbed from c-Ca_2SiO_4/C-Ag/GO and s-Ca_2SiO_4/C-Ag-GO scaffolds under bactericidal test conditions.

PBS under bactericidal test conditions. Fig. 9 shows the total silver concentrations measured in the PBS solutions obtained.

In the case of c-Ca_2SiO_4/C-Ag/GO, 0.32 ± 0.06 mg L^{-1} of silver was desorbed while 0.11 ± 0.02 mg L^{-1} was released by s-Ca_2SiO_4/C-Ag/GO (Fig. 9). Thanks to ICP-MS, the silver released was estimated to represent 11% w/w (for c-Ca_2SiO_4/C-Ag/GO) and 17% w/w (for s-Ca_2SiO_4/C-Ag/GO) of the total silver incorporated into the ceramics. The s-Ca_2SiO_4/C material demonstrates excellent surface chemical stability, coupled with effective dispersion and fixation of silver nanoparticles (Fig. 8). Notably, no bactericidal activity was observed upon desorption of silver in both scenarios. This outcome can be attributed to the minimal amount of silver released. Consequently, it is inferred that the antibacterial efficacy showcased in Fig. 7 is directly linked to the presence of silver on the ceramic surface.

In order to demonstrate the activity of GO (not significant at high bacterial concentration, Section 3.5), bactericidal tests in liquid medium were performed in exactly the same way as the previous tests, but using a lower initial bacterial concentration (*i.e.* 1.1 ± 0.0 × 10^4 CFU mL^{-1} *vs.* 1.8 ± 0.8 × 10^7 CFU mL^{-1}). Bacterial concentration C (CFU mL^{-1}) was measured initially and at the end of the incubation as described in Section 2.6.2.

Fig. 10 shows the *E. coli* removals obtained after 3 h of contact with the different scaffolds. Compared to the blank, we can still see that the s-Ca_2SiO_4 ceramic scaffolds have no antibacterial activity, while the c-Ca_2SiO_4/C scaffolds show a slight decrease in the bacteria concentration (−0.1 log removal) which could be attributed to bacterial adsorption. The c-Ca_2SiO_4/C-GO and s-Ca_2SiO_4-GO scaffolds produced more significant log removal values than with a high initial bacterial concentration (−0.4 and −0.2 *vs.* 0 and −0.1, respectively). This suggests that GO exhibits moderate bactericidal activity at low bacterial concentration. Furthermore, lowering the initial bacterial concentration induced a significant increase of the *E. coli* removal by s-Ca_2SiO_4 scaffolds (−2.6 ± 0.0 *vs.* −1.1 ± 0.2). Similarly, the bacterial reduction enabled by c-Ca_2SiO_4/C-Ag/GO scaffolds increased to −1.6 ± 0.1 (*vs.* −0.40 ± 0.02). The decrease in bacterial concentration suggests a relative bactericidal activity of GO. However, this effect alone is not sufficient hence the need to use silver to confer significant antibacterial activity to the materials.

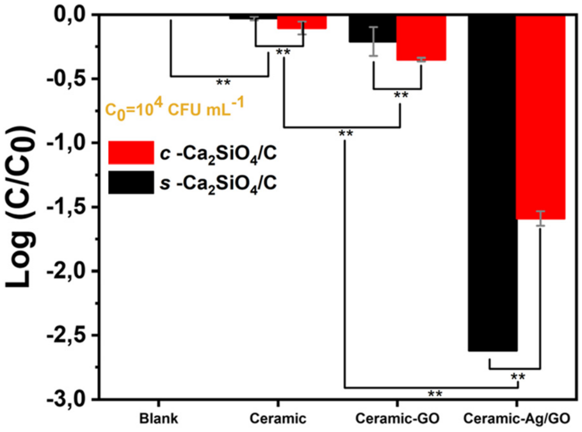

Fig. 10 *E. coli* removal by scaffolds: ceramic; GO and Ag/GO functionalized ceramics. C_0 is the initial bacterial concentration (1.0 ± 0.0 × 10^4 CFU mL^{-1}) and C (CFU mL^{-1}) the concentration of bacteria measured after 3 h incubation. **($p < 0.05$) indicates a significant difference between the different materials and conditions.

3.6. Degradation and apatite mineralization ability of scaffolds

Fig. 11(a) and (b) show the weight loss of both types of scaffold as a function of pH changes in the scaffold environment. The change in pH is due to the release of ceramic elements into the SBF solution. It can be seen that SBF pH values increase with soaking time. After 7 days soaking, the pH values of c-Ca_2SiO_4/C and s-Ca_2SiO_4/C scaffolds were 8.5 ± 0.007, 8.2 ± 0.002 respectively. Consequently, weight loss clearly occurred for each scaffold type due to the degradability of these scaffolds. After soaking in SBF for 4 weeks, the residual weights of c-Ca_2SiO_4/C and s-Ca_2SiO_4/C scaffolds were 50.53 ± 0.07, 68.3 ± 0.14, respectively. The s-Ca_2SiO_4/C scaffold exhibited a slower degradability rate than the c-Ca_2SiO_4/C scaffold, which may be explained by a better structural stability that may influence its time-dependent behavior in SBF. The formation of apatite on the scaffolds after soaking in SBF was observed by SEM. As shown in Fig. 11(c) and (d), both scaffolds retained the interconnected macroporous structure after 7 days soaking in SBF, but the surface of the scaffolds became much rougher, due to the formation of a thin layer of apatite on their surface. In addition, increasing the soaking time improved the rate of apatite deposition on the larnite surface. The surface of the scaffolds was completely covered with apatite by day 7, indicating their excellent biomineralization ability. This is due to the high calcium content present in these ceramic materials compared with other bioactive materials (*e.g.* wollastonite).[94] In addition, the presence of silicon in a sufficient amount stimulates the deposition of apatite on the surface.[1] Moreover, EDX analysis revealed the presence of calcium, oxygen and phosphorus, the main constituents of hydroxyapatite. The Ca/P ratio of the c-Ca_2SiO_4/C and s-Ca_2SiO_4/C scaffolds surface was 1.94 and 2.25, respectively.

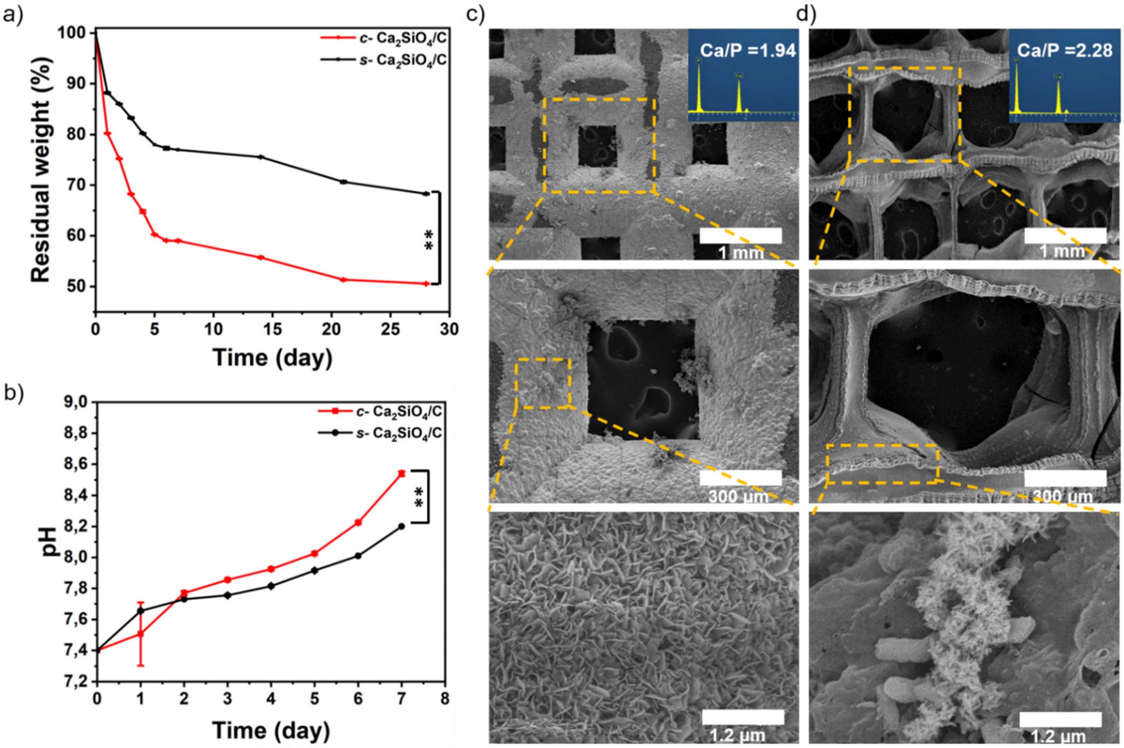

Fig. 11 *In vitro* tests: (a) degradation and (b) pH values of c-Ca_2SiO_4/C and s-Ca_2SiO_4/C ceramic scaffolds in SBF (**($p < 0.05$) indicate significant difference), SEM images (c) of c-Ca_2SiO_4/C and (d) s-Ca_2SiO_4/C scaffolds after immersion in SBF for 7 days; EDX analysis of these scaffolds after immersion in SBF for 7 days.

The Ca/P ratio in the case of s-Ca_2SiO_4/C is higher than that of c-Ca_2SiO_4/C, and this can be explained by the thinner layer formed on its surface, which allowed the calcium to be detected. This thin layer formed after 7 days immersion in SBF is evidenced by a lower degradation rate and a smaller pH value.

3.7. Cell proliferation and cytotoxicity

The proliferation of BM-MSCs is an essential property for assessing the quality of biomaterials intended for tissue engineering. To this end, BM-MSCs were cultured on bioceramics for 7 days and the proliferation rate of BM-MSCs was assessed. The results showed that all bioceramics significantly accelerated the proliferation rate of MSCs compared with the control group ($p < 0.05$) (Fig. 12(a)). Interestingly, both uncoated group c-Ca_2SiO_4/C and s-Ca_2SiO_4/C bioceramics stimulated the proliferative effect of BM-MSCs and showed significant differences compared with the control group. In contrast, this pattern was not observed in the group

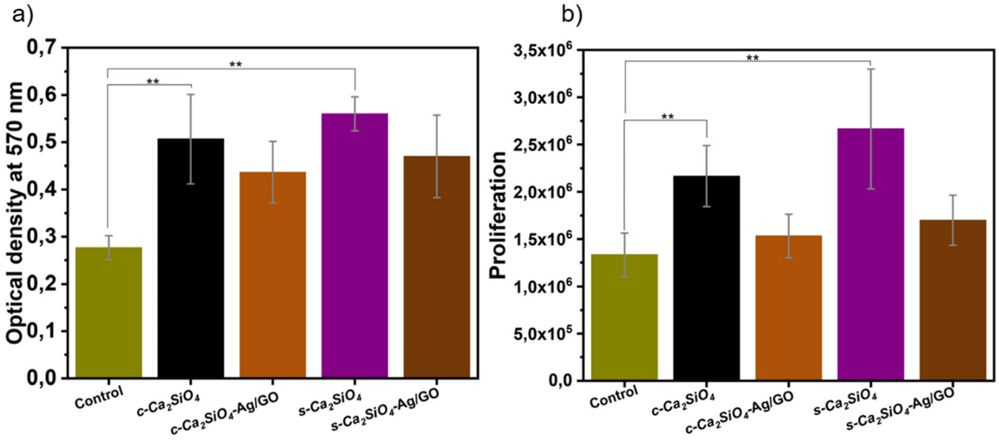

Fig. 12 (a) Cellular proliferation activity of BM-MSCs for bioceramics (c-Ca_2SiO_4/C, c-Ca_2SiO_4/C-Ag/GO, s-Ca_2SiO_4/C and s-Ca_2SiO_4/C-Ag/GO) cultured at 7 days. (b) MTT viability assay of BM-MSCs cultured at 7 days on c-Ca_2SiO_4/C, c-Ca_2SiO_4/C-Ag/GO, s-Ca_2SiO_4/C and s-Ca_2SiO_4/C-Ag/GO bioceramics. Bars represent standard deviations and ** represents significant differences between the bracketed pair group.

c-Ca_2SiO_4/C and s-Ca_2SiO_4/C coated with Ag/GO, where the proliferative effect of the bioceramics decreased with Ag/GO coating, while remaining higher than that of the control group.

Cytotoxic results showed that cells cultured on all bioceramics had a significantly higher OD value at 570 nm than the control ($p < 0.05$) (Fig. 12(b)). Among the samples tested, biocompatibility of bioceramics was slightly reduced by the Ag/GO coating, but the differences were not significant. Interestingly, cells cultured on c-Ca_2SiO_4/C and s-Ca_2SiO_4/C had a cytocompatibility rate 2 to 3 times higher than control cells.[27,85,89,90] After 7 days in culture, BM-MSCs showed a well-distributed morphology on each type of scaffold with no obvious differences. However, the proliferation rate of BM-MSCs increased with time. This clearly indicates that bioceramic scaffolds promote cell adhesion and viability.[95] Indeed, BM-MSCs proliferation was significantly higher on c-Ca_2SiO_4/C and s-Ca_2SiO_4/C with significant differences ($p < 0.05$), which is in full agreement with the literature.[36,96,97] These results are also in agreement with those of Fu *et al.* who reported the proliferation of rat bone mesenchymal stem cells (rBMSCs) at 7 days of culture, on 3D printed porous β-Ca_2SiO_4. They also reported significant differences in cells cultured on β-Ca_2SiO_4 scaffolds sintered at 1000 °C at day 7 compared with the control.[36]

4. Conclusions

In this work, we have introduced for the first time the use of vat photopolymerization technology to fabricate three-dimensional (3D) porous β-Ca_2SiO_4 ceramic scaffolds functionalized with silver nanoparticles (AgNPs) decorated graphene oxide (GO). These scaffolds were obtained from either commercial resin blends or "customized" silicone resin both loaded with $CaCO_3$ particles. Ceramics annealed at 1200 °C showed improved relative density, which also enhanced compressive strength. β-Ca_2SiO_4 ceramics scaffolds showed good *in vitro* bioactivity. According to our results, ceramics fabricated from "customized" resin and functionalized with Ag/GO nanoparticles showed significant antibacterial activity against *E. coli*. As a result, these scaffolds proved their biocompatibility *in vitro* using mesenchymal stem cells (MSCs) culture, thanks to their low cytotoxicity and accelerated MSCs proliferation rate compared to the control. Overall, due to their interconnected porosity, excellent biomineralization, cytocompatibility, mechanical and antibacterial properties, these 3D printed antibacterial scaffolds would be promising candidates for bone tissue engineering.

Author contributions

C. S.: conceptualization, methodology, validation, investigation, resources, writing – review & editing, visualization, supervision, project administration, funding acquisition. L. S.: investigation, resources, methodology, data curation, writing – review & editing. M. Z.: supervision, funding acquisition, writing – review & editing. P. M.: supervision, writing – review & editing. D. V.: resources, investigation, writing – review & editing. M. N.: supervision, funding acquisition, writing – review & editing. M. B. C. Z. L.: investigation, resources, validation, visualization. J. E.: investigation, validation, visualization. C. G.: investigation, resources, validation. I. I.: investigation, resources, validation, visualization. E. C.: investigation, validation, visualization. G. E. C.: investigation. L. C. d. S. C.: investigation. H. B.: investigation. J. E. H.: investigation, data curation, validation, visualization, formal analysis, writing – original draft.

Conflicts of interest

There are no conflicts to declare.

Acknowledgements

C. S. acknowledges funding from the French National Agency (ANR), Grant Number: ANR-20-CE08-0009 (MONOME project). C. S., M. Z. and M. N. acknowledge the partial financial support from the Lebanese University. I. I. acknowledges the partial financial support from the National Science Centre of Poland from the OPUS project 2020/37/B/ST5/00576.

References

1 W. Cao and L. L. Hench, Bioactive Materials, *Ceram. Int.*, 1996, **22**, 493–507.
2 R. Kumar, I. Pattanayak, P. A. Dash and S. Mohanty, Bioceramics: A Review on Design Concepts toward Tailor-Made (Multi)-Functional Materials for Tissue Engineering Applications, *J. Mater. Sci.*, 2023, **58**, 3460–3484.
3 C. Wu, Y. Zhou, C. Lin, J. Chang and Y. Xiao, Strontium-Containing Mesoporous Bioactive Glass Scaffolds with Improved Osteogenic/Cementogenic Differentiation of Periodontal Ligament Cells for Periodontal Tissue Engineering, *Acta Biomater.*, 2012, **8**, 3805–3815.
4 E. Ellermann, N. Meyer, R. E. Cameron and S. M. Best, In Vitro Angiogenesis in Response to Biomaterial Properties for Bone Tissue Engineering: A Review of the State of the Art, *Regen. Biomater.*, 2023, **10**, rbad027.
5 R. Kuijer, E. J. Jansen, P. J. Emans, S. K. Bulstra, J. Riesle, J. Pieper, D. W. Grainger and H. J. Busscher, Assessing Infection Risk in Implanted Tissue-Engineered Devices, *Biomaterials*, 2007, **28**, 5148–5154.
6 Y. Tang, Y. Zhao, H. Wang, Y. Gao, X. Liu, X. Wang and T. Lin, Layer-by-Layer Assembly of Antibacterial Coating on Interbonded 3D Fibrous Scaffolds and Its Cytocompatibility Assessment, *J. Biomed. Mater. Res., Part A*, 2012, **100**, 2071–2078.
7 X. Ren, X. Chen, Z. Geng and J. Su, Bone-Targeted Biomaterials: Strategies and Applications, *Chem. Eng. J.*, 2022, **446**, 137133, DOI: 10.1016/j.cej.2022.137133.
8 G. Wang, Z. Yuan, L. Yu, Y. Yu, P. Zhou, G. Chu, H. Wang, Q. Guo, C. Zhu and F. Han, *et al.*, Mechanically Conditioned Cell Sheets Cultured on Thermo-Responsive Surfaces

Promote Bone Regeneration, *Biomater. Transl.*, 2023, **4**, 27–40, DOI: **10.12336/biomatertransl.2023.01.005**.

9 E. Steijvers, A. Ghei and Z. Xia, Manufacturing Artificial Bone Allografts: A Perspective, *Biomater. Transl.*, 2022, **3**, 65–80, DOI: **10.12336/biomatertransl.2022.01.007**.

10 Y. Ramaswamy, C. Wu, H. Zhou and H. Zreiqat, Biological Response of Human Bone Cells to Zinc-Modified Ca–Si-Based Ceramics, *Acta Biomater.*, 2008, **4**, 1487–1497.

11 C. Wu, Y. Ramaswamy, P. Boughton and H. Zreiqat, Improvement of Mechanical and Biological Properties of Porous $CaSiO_3$ Scaffolds by Poly (D, L-Lactic Acid) Modification, *Acta Biomater.*, 2008, **4**, 343–353.

12 C. Wu, Y. Ramaswamy and H. Zreiqat, Porous Diopside ($CaMgSi_2O_6$) Scaffold: A Promising Bioactive Material for Bone Tissue Engineering, *Acta Biomater.*, 2010, **6**, 2237–2245.

13 M. Zhu, J. Zhang, S. Zhao and Y. Zhu, Three-Dimensional Printing of Cerium-Incorporated Mesoporous Calcium-Silicate Scaffolds for Bone Repair, *J. Mater. Sci.*, 2016, **51**, 836–844.

14 M.-Y. Shie, S.-J. Ding and H.-C. Chang, The Role of Silicon in Osteoblast-like Cell Proliferation and Apoptosis, *Acta Biomater.*, 2011, **7**, 2604–2614.

15 J. Sun, L. Wei, X. Liu, J. Li, B. Li, G. Wang and F. Meng, Influences of Ionic Dissolution Products of Dicalcium Silicate Coating on Osteoblastic Proliferation, Differentiation and Gene Expression, *Acta Biomater.*, 2009, **5**, 1284–1293.

16 P. J. Bártolo, H. Almeida and T. Laoui, Rapid Prototyping and Manufacturing for Tissue Engineering Scaffolds, *Int. J. Comput. Appl. Technol.*, 2009, **36**, 1–9.

17 L. Fiocco, H. Elsayed, D. Badocco, P. Pastore, D. Bellucci, V. Cannillo, R. Detsch, A. R. Boccaccini and E. Bernardo, Direct Ink Writing of Silica-Bonded Calcite Scaffolds from Preceramic Polymers and Fillers, *Biofabrication*, 2017, **9**, 025012.

18 L. Fiocco, S. Agnoli, D. Pedron, M. Secco, S. Tamburini, L. Ferroni, C. Gardin, B. Zavan and E. Bernardo, Wollastonite-Diopside-Carbon Composite Foams from a Silicone Resin and Inorganic Fillers, *Ceram. Int.*, 2018, **44**, 931–937.

19 E. Bernardo, J.-F. Carlotti, P. M. Dias, L. Fiocco, P. Colombo, L. Treccani, U. Hess and K. Rezwan, Novel Akermanite-Based Bioceramics from Preceramic Polymers and Oxide Fillers, *Ceram. Int.*, 2014, **40**, 1029–1035.

20 C. Wu, J. Chang, W. Zhai, S. Ni and J. Wang, Porous Akermanite Scaffolds for Bone Tissue Engineering: Preparation, Characterization, and in Vitro Studies, *J. Biomed. Mater. Res., Part B*, 2006, **78**, 47–55.

21 A. Zocca, G. Franchin, H. Elsayed, E. Gioffredi, E. Bernardo and P. Colombo, Direct Ink Writing of a Preceramic Polymer and Fillers to Produce Hardystonite ($Ca_2ZnSi_2O_7$) Bioceramic Scaffolds, *J. Am. Ceram. Soc.*, 2016, **99**, 1960–1967.

22 E. Bernardo, E. Tomasella and P. Colombo, Development of Multiphase Bioceramics from a Filler-Containing Preceramic Polymer, *Ceram. Int.*, 2009, **35**, 1415–1421.

23 C. Wu, J. Chang, W. Zhai and S. Ni, A Novel Bioactive Porous Bredigite ($Ca_7MgSi_4O_{16}$) Scaffold with Biomimetic Apatite Layer for Bone Tissue Engineering, *J. Mater. Sci.: Mater. Med.*, 2007, **18**, 857–864.

24 Y. Huang, C. Wu, X. Zhang, J. Chang and K. Dai, Regulation of Immune Response by Bioactive Ions Released from Silicate Bioceramics for Bone Regeneration, *Acta Biomater.*, 2018, **66**, 81–92.

25 J. Kulhánková, D. Rohanová, D. Horkavcová, P. Bezdička and A. R. Boccaccini, The Role of (HCO_3)- Ions in SBF on the Interaction with Bioactive Glass-Ceramic Scaffold, *Mater. Today Chem.*, 2023, **28**, 101367.

26 Y. Dai, H. Liu, B. Liu, Z. Wang, Y. Li and G. Zhou, Porous β-Ca_2SiO_4 Ceramic Scaffolds for Bone Tissue Engineering: In Vitro and in Vivo Characterization, *Ceram. Int.*, 2015, **41**, 5894–5902.

27 R. Choudhary, S. K. Venkatraman, A. Rana and S. Swamiappan, In Vitro Bioactivity Studies of Larnite and Larnite/Chitin Composites Prepared from Biowaste for Biomedical Applications, *Bull. Mater. Sci.*, 2016, **39**, 1213–1221.

28 Q. Fu, E. Saiz, M. N. Rahaman and A. P. Tomsia, Bioactive Glass Scaffolds for Bone Tissue Engineering: State of the Art and Future Perspectives, *Mater. Sci. Eng., C*, 2011, **31**, 1245–1256.

29 F. Baino and C. Vitale-Brovarone, Bioceramics in Ophthalmology, *Acta Biomater.*, 2014, **10**, 3372–3397.

30 Y. S. Cho, S. Choi, S.-H. Lee, K. K. Kim and Y.-S. Cho, Assessments of Polycaprolactone/Hydroxyapatite Composite Scaffold with Enhanced Biomimetic Mineralization by Exposure to Hydroxyapatite via a 3D-Printing System and Alkaline Erosion, *Eur. Polym. J.*, 2019, **113**, 340–348.

31 F. Matassi, L. Nistri, D. C. Paez and M. Innocenti, New Biomaterials for Bone Regeneration, *Clin. Cases Miner. Bone Metab.*, 2011, **8**, 21.

32 P. Madani, S. Hesaraki, M. Saeedifar and N. Ahmadi Nasab, The Controlled Release, Bioactivity and Osteogenic Gene Expression of Quercetin-Loaded Gelatin/Tragacanth/Nano-Hydroxyapatite Bone Tissue Engineering Scaffold, *J. Biomater. Sci. Polym. Ed.*, 2023, **34**, 217–242, DOI: **10.1080/09205063.2022.2113293**.

33 B. Tan, N. Zhao, W. Guo, F. Huang, H. Hu, Y. Chen, J. Li, Z. Ling, Z. Zou and R. Hu, Biomimetic Hydroxyapatite Coating on the 3D-Printed Bioactive Porous Composite Ceramic Scaffolds Promoted Osteogenic Differentiation via PI3K/AKT/mTOR Signaling Pathways and Facilitated Bone Regeneration in Vivo, *J. Mater. Sci. Technol.*, 2023, **136**, 54–64.

34 I. López-González, C. Zamora-Ledezma, M. I. Sanchez-Lorencio, E. Tristante Barrenechea, J. A. Gabaldón-Hernández and L. Meseguer-Olmo, Modifications in Gene Expression in the Process of Osteoblastic Differentiation of Multipotent Bone Marrow-Derived Human Mesenchymal Stem Cells Induced by a Novel Osteoinductive Porous Medical-Grade 3D-Printed Poly (ε-Caprolactone)/β-Tricalcium Phosphate Composite, *Int. J. Mol. Sci.*, 2021, **22**, 11216.

35 V. Baumer, E. Gunn, V. Riegle, C. Bailey, C. Shonkwiler and D. Prawel, Robocasting of Ceramic Fischer–Koch S Scaffolds for Bone Tissue Engineering, *J. Funct. Biomater.*, 2023, **14**, 251.

36 S. Fu, W. Liu, S. Liu, S. Zhao and Y. Zhu, 3D Printed Porous β-Ca_2SiO_4 Scaffolds Derived from Preceramic Resin and

Their Physicochemical and Biological Properties, *Sci. Technol. Adv. Mater.*, 2018, **19**, 495–506.

37 S.-Y. Fu, B. Yu, H.-F. Ding, G.-D. Shi and Y.-F. Zhu, Zirconia Incorporation in 3D Printed β-Ca_2SiO_4 Scaffolds on Their Physicochemical and Biological Property, *J. Inorg. Mater.*, 2019, **34**, 4.

38 B. Yu, S. Fu, Z. Kang, M. Zhu, H. Ding, T. Luo, Y. Zhu and Y. Zhang, Enhanced Bone Regeneration of 3D Printed β-Ca_2SiO_4 Scaffolds by Aluminum Ions Solid Solution, *Ceram. Int.*, 2020, **46**, 7783–7791.

39 E. S. Bishop, S. Mostafa, M. Pakvasa, H. H. Luu, M. J. Lee, J. M. Wolf, G. A. Ameer, T.-C. He and R. R. Reid, 3-D Bioprinting Technologies in Tissue Engineering and Regenerative Medicine: Current and Future Trends, *Genes Dis.*, 2017, **4**, 185–195.

40 A. P. M. Madrid, S. M. Vrech, M. A. Sanchez and A. P. Rodriguez, Advances in Additive Manufacturing for Bone Tissue Engineering Scaffolds, *Mater. Sci. Eng., C*, 2019, **100**, 631–644.

41 N. Ajmal, S. Z. Khan and R. Shaikh, Polycystic Ovary Syndrome (PCOS) and Genetic Predisposition: A Review Article, *Eur. J. Obstet. Gynecol. Reprod. Biol. X*, 2019, **3**, 100060.

42 F. Baino, G. Magnaterra, E. Fiume, A. Schiavi, L.-P. Tofan, M. Schwentenwein and E. Verné, Digital Light Processing Stereolithography of Hydroxyapatite Scaffolds with Bone-like Architecture, Permeability, and Mechanical Properties, *J. Am. Ceram. Soc.*, 2022, **105**, 1648–1657.

43 Z. Wang, C. Huang, J. Wang and B. Zou, Development of a Novel Aqueous Hydroxyapatite Suspension for Stereolithography Applied to Bone Tissue Engineering, *Ceram. Int.*, 2019, **45**, 3902–3909.

44 L. Ferrage, G. Bertrand, P. Lenormand, D. Grossin and B. Ben-Nissan, A Review of the Additive Manufacturing (3DP) of Bioceramics: Alumina, Zirconia (PSZ) and Hydroxyapatite, *J. Aust. Ceram. Soc.*, 2017, **53**, 11–20.

45 R. Liu, L. Ma, H. Liu, B. Xu, C. Feng and R. He, Effects of Pore Size on the Mechanical and Biological Properties of Stereolithographic 3D Printed HAp Bioceramic Scaffold, *Ceram. Int.*, 2021, **47**, 28924–28931.

46 Z. Wang, C. Huang, J. Wang, B. Zou, C. A. Abbas and X. Wang, Design and Characterization of Hydroxyapatite Scaffolds Fabricated by Stereolithography for Bone Tissue Engineering Application, *Procedia CIRP*, 2020, **89**, 170–175.

47 P. Navarrete-Segado, M. Tourbin, C. Frances and D. Grossin, Masked Stereolithography of Hydroxyapatite Bioceramic Scaffolds: From Powder Tailoring to Evaluation of 3D Printed Parts Properties, *Open Ceram.*, 2022, **9**, 100235.

48 C. Feng, K. Zhang, R. He, G. Ding, M. Xia, X. Jin and C. Xie, Additive Manufacturing of Hydroxyapatite Bioceramic Scaffolds: Dispersion, Digital Light Processing, Sintering, Mechanical Properties, and Biocompatibility, *J. Adv. Ceram.*, 2020, **9**, 360–373.

49 Y. Wei, D. Zhao, Q. Cao, J. Wang, Y. Wu, B. Yuan, X. Li, X. Chen, Y. Zhou and X. Yang, Stereolithography-Based Additive Manufacturing of High-Performance Osteoinductive Calcium Phosphate Ceramics by a Digital Light-Processing System, *ACS Biomater. Sci. Eng.*, 2020, **6**, 1787–1797.

50 W. Bian, D. Li, Q. Lian, W. Zhang, L. Zhu, X. Li and Z. Jin, Design and Fabrication of a Novel Porous Implant with Pre-Set Channels Based on Ceramic Stereolithography for Vascular Implantation, *Biofabrication*, 2011, **3**, 034103.

51 T. Zhou, L. Zhang, Q. Yao, Y. Ma, C. Hou, B. Sun, C. Shao, P. Gao and H. Chen, SLA 3D Printing of High Quality Spine Shaped β-TCP Bioceramics for the Hard Tissue Repair Applications, *Ceram. Int.*, 2020, **46**, 7609–7614.

52 X. Huang, H. Dai, Y. Hu, P. Zhuang, Z. Shi and Y. Ma, Development of a High Solid Loading β-TCP Suspension with a Low Refractive Index Contrast for DLP-Based Ceramic Stereolithography, *J. Eur. Ceram. Soc.*, 2021, **41**, 3743–3754.

53 N. Rangelova, L. Aleksandrov, T. Angelova, N. Georgieva and R. Müller, Preparation and Characterization of SiO2/CMC/Ag Hybrids with Antibacterial Properties, *Carbohydr. Polym.*, 2014, **101**, 1166–1175.

54 F. Lu, R. Wu, M. Shen, L. Xie, M. Liu, Y. Li, S. Xu, L. Wan, X. Yang and C. Gao, Rational Design of Bioceramic Scaffolds with Tuning Pore Geometry by Stereolithography: Microstructure Evaluation and Mechanical Evolution, *J. Eur. Ceram. Soc.*, 2021, **41**, 1672–1682.

55 Y. Li, R. Wu, L. Yu, M. Shen, X. Ding, F. Lu, M. Liu, X. Yang, Z. Gou and S. Xu, Rational Design of Nonstoichiometric Bioceramic Scaffolds via Digital Light Processing: Tuning Chemical Composition and Pore Geometry Evaluation, *J. Biol. Eng.*, 2021, **15**, 1–12.

56 J. Schmidt, H. Elsayed, E. Bernardo and P. Colombo, Digital Light Processing of Wollastonite-Diopside Glass-Ceramic Complex Structures, *J. Eur. Ceram. Soc.*, 2018, **38**, 4580–4584.

57 A. Dasan, J. Kraxner, L. Grigolato, G. Savio, H. Elsayed, D. Galusek and E. Bernardo, 3D Printing of Hierarchically Porous Lattice Structures Based on Åkermanite Glass Microspheres and Reactive Silicone Binder, *J. Funct. Biomater.*, 2022, **13**, 8.

58 N. Travitzky, A. Bonet, B. Dermeik, T. Fey, I. Filbert-Demut, L. Schlier, T. Schlordt and P. Greil, Additive Manufacturing of Ceramic-Based Materials, *Adv. Eng. Mater.*, 2014, **16**, 729–754.

59 J. W. Halloran, V. Tomeckova, S. Gentry, S. Das, P. Cilino, D. Yuan, R. Guo, A. Rudraraju, P. Shao and T. Wu, Photopolymerization of Powder Suspensions for Shaping Ceramics, *J. Eur. Ceram. Soc.*, 2011, **31**, 2613–2619.

60 Y. De Hazan, J. Heinecke, A. Weber and T. Graule, High Solids Loading Ceramic Colloidal Dispersions in UV Curable Media via Comb-Polyelectrolyte Surfactants, *J. Colloid Interface Sci.*, 2009, **337**, 66–74.

61 W. Liu, R. Zuo, T. Zhu, M. Zhu, S. Zhao and Y. Zhu, Forsterite-Hydroxyapatite Composite Scaffolds with Photothermal Antibacterial Activity for Bone Repair, *J. Adv. Ceram.*, 2021, **10**, 1095–1106.

62 V. V. Nayak, N. Tovar, J. H. Hacquebord, S. Duarte, B. H. Panariello, C. Tonon, P. J. Atria, P. G. Coelho and L. Witek, Physiochemical and Bactericidal Activity Evaluation: Silver-

Augmented 3D-Printed Scaffolds—An in Vitro Study, *J. Biomed. Mater. Res., Part B*, 2022, **110**, 195–209.

63 Y. Zhang, D. Zhai, M. Xu, Q. Yao, H. Zhu, J. Chang and C. Wu, 3D-Printed Bioceramic Scaffolds with Antibacterial and Osteogenic Activity, *Biofabrication*, 2017, **9**, 025037.

64 J. Wang, Y. Peng, M. Chen, X. Dai, L. Lou, C. Wang, Z. Bao, X. Yang, Z. Gou and J. Ye, Next-Generation Finely Controlled Graded Porous Antibacterial Bioceramics for High-Efficiency Vascularization in Orbital Reconstruction, *Bioact. Mater.*, 2022, 334–345.

65 J. Wang, C. Wang, K. Jin, X. Yang, L. Gao, C. Yao, X. Dai, J. He, C. Gao and J. Ye, Simultaneous Enhancement of Vascularization and Contact-Active Antibacterial Activity in Diopside-Based Ceramic Orbital Implants, *Mater. Sci. Eng., C*, 2019, **105**, 110036.

66 S.-S. Choi, A. S. Lee, H. S. Lee, H. Y. Jeon, K.-Y. Baek, D. H. Choi and S. S. Hwang, Synthesis and Characterization of UV-Curable Ladder-like Polysilsesquioxane, *J. Polym. Sci. Part. Polym. Chem.*, 2011, **49**, 5012–5018.

67 J. D. Padmos, M. Langman, K. MacDonald, P. Comeau, Z. Yang, M. Filiaggi and P. Zhang, Correlating the Atomic Structure of Bimetallic Silver–Gold Nanoparticles to Their Antibacterial and Cytotoxic Activities, *J. Phys. Chem. C*, 2015, **119**, 7472–7482.

68 Z. Fan, B. Liu, J. Wang, S. Zhang, Q. Lin, P. Gong, L. Ma and S. Yang, A Novel Wound Dressing Based on Ag/Graphene Polymer Hydrogel: Effectively Kill Bacteria and Accelerate Wound Healing, *Adv. Funct. Mater.*, 2014, **24**, 3933–3943.

69 W. S. Hummers Jr and R. E. Offeman, Preparation of Graphitic Oxide, *J. Am. Chem. Soc.*, 1958, **80**, 1339.

70 P. Kamgang-Syapnjeu, D. Njoya, E. Kamseu, L. C. de Saint Cyr, A. Marcano-Zerpa, S. Balme, M. Bechelany and L. Soussan, Elaboration of a New Ceramic Membrane Support from Cameroonian Clays, Coconut Husks and Eggshells: Application for Escherichia Coli Bacteria Retention, *Appl. Clay Sci.*, 2020, **198**, 105836.

71 T. Kokubo and H. Takadama, How Useful Is SBF in Predicting in Vivo Bone Bioactivity?, *Biomaterials*, 2006, **27**, 2907–2915.

72 J. Elango, R. Bushin, A. Lijnev, P. N. De Aza, C. P.-A. Martínez, J. M. G. Marín, A. B. Hernandez, L. R. M. Olmo and J. E. M. S. D. Val, The Effect of Germanium-Loaded Hydroxyapatite Biomaterials on Bone Marrow Mesenchymal Stem Cells Growth, *Cells*, 2022, **11**, 2993.

73 L. Zhang, D. Dai and R. Zhang, The Synthesis and X-Ray Diffraction Study of the Ladder-like Polysilsesquioxanes with Side-Chain Ester Groups, *Polym. Adv. Technol.*, 1997, **8**, 662–665.

74 S. Chernousova and M. Epple, Silver as Antibacterial Agent: Ion, Nanoparticle, and Metal, *Angew. Chem., Int. Ed.*, 2013, **52**, 1636–1653.

75 M. Rai, A. Yadav and A. Gade, Silver Nanoparticles as a New Generation of Antimicrobials, *Biotechnol. Adv.*, 2009, **27**, 76–83.

76 W.-P. Xu, L.-C. Zhang, J.-P. Li, Y. Lu, H.-H. Li, Y.-N. Ma, W.-D. Wang and S.-H. Yu, Facile Synthesis of Silver@ Graphene Oxide Nanocomposites and Their Enhanced Antibacterial Properties, *J. Mater. Chem.*, 2011, **21**, 4593–4597.

77 T. Angelova, N. Rangelova, R. Yuryev, N. Georgieva and R. Müller, Antibacterial Activity of SiO2/Hydroxypropyl Cellulose Hybrid Materials Containing Silver Nanoparticles, *Mater. Sci. Eng., C*, 2012, **32**, 1241–1246.

78 M. J. Hajipour, K. M. Fromm, A. A. Ashkarran, D. J. de Aberasturi, I. R. de Larramendi, T. Rojo, V. Serpooshan, W. J. Parak and M. Mahmoudi, Antibacterial Properties of Nanoparticles, *Trends Biotechnol.*, 2012, **30**, 499–511.

79 F. Furno, K. S. Morley, B. Wong, B. L. Sharp, P. L. Arnold, S. M. Howdle, R. Bayston, P. D. Brown, P. D. Winship and H. J. Reid, Silver Nanoparticles and Polymeric Medical Devices: A New Approach to Prevention of Infection?, *J. Antimicrob. Chemother.*, 2004, **54**, 1019–1024.

80 J. S. Kim, E. Kuk, K. N. Yu, J.-H. Kim, S. J. Park, H. J. Lee, S. H. Kim, Y. K. Park, Y. H. Park and C.-Y. Hwang, Antimicrobial Effects of Silver Nanoparticles, *Nanomed. Nanotechnol. Biol. Med.*, 2007, **3**, 95–101.

81 J. I. Paredes, S. Villar-Rodil, A. Martínez-Alonso and J. M. D. Tascon, Graphene Oxide Dispersions in Organic Solvents, *Langmuir*, 2008, **24**, 10560–10564.

82 D. D. Evanoff Jr and G. Chumanov, Synthesis and Optical Properties of Silver Nanoparticles and Arrays, *ChemPhysChem*, 2005, **6**, 1221–1231.

83 S. W. Chook, C. H. Chia, S. Zakaria, M. K. Ayob, K. L. Chee, N. M. Huang, H. M. Neoh, H. N. Lim, R. Jamal and R. Rahman, Antibacterial Performance of Ag Nanoparticles and AgGO Nanocomposites Prepared via Rapid Microwave-Assisted Synthesis Method, *Nanoscale Res. Lett.*, 2012, **7**, 1–7.

84 D. Li, M. B. Müller, S. Gilje, R. B. Kaner and G. G. Wallace, Processable Aqueous Dispersions of Graphene Nanosheets, *Nat. Nanotechnol.*, 2008, **3**, 101–105.

85 J. Li and C. Liu, Ag/Graphene Heterostructures: Synthesis, Characterization and Optical Properties, *Eur. J. Inorg. Chem.*, 2010, 1244–1248.

86 J. Shen, T. Li, M. Shi, N. Li and M. Ye, Polyelectrolyte-Assisted One-Step Hydrothermal Synthesis of Ag-Reduced Graphene Oxide Composite and Its Antibacterial Properties, *Mater. Sci. Eng., C*, 2012, **32**, 2042–2047.

87 S. You, S. M. Luzan, T. Szabó and A. V. Talyzin, Effect of Synthesis Method on Solvation and Exfoliation of Graphite Oxide, *Carbon*, 2013, **52**, 171–180.

88 S.-K. Li, Y.-X. Yan, J.-L. Wang and S.-H. Yu, Bio-Inspired in Situ Growth of Monolayer Silver Nanoparticles on Graphene Oxide Paper as Multifunctional Substrate, *Nanoscale*, 2013, **5**, 12616–12623.

89 F. Tuinstra and J. L. Koenig, Raman Spectrum of Graphite, *J. Chem. Phys.*, 1970, **53**, 1126–1130.

90 B. Jiang, C. Tian, G. Song, W. Chang, G. Wang, Q. Wu and H. Fu, A Novel Ag/Graphene Composite: Facile Fabrication and Enhanced Antibacterial Properties, *J. Mater. Sci.*, 2013, **48**, 1980–1985.

91 M. Yan, W. Song and C. Zhao-hui, Raman Spectroscopy Studies of the High-Temperature Evolution of the Free Carbon Phase in Polycarbosilane Derived SiC Ceramics, *Ceram. Int.*, 2010, **36**, 2455–2459.

92 I. Gonzalo-Juan, R. Detsch, S. Mathur, E. Ionescu, A. R. Boccaccini and R. Riedel, Synthesis and in Vitro Activity

Assessment of Novel Silicon Oxycarbide-Based Bioactive Glasses, *Materials*, 2016, **9**, 959.

93 S. Zheng, M. Bawazir, A. Dhall, H.-E. Kim, L. He, J. Heo and G. Hwang, Implication of Surface Properties, Bacterial Motility, and Hydrodynamic Conditions on Bacterial Surface Sensing and Their Initial Adhesion, *Front. Bioeng. Biotechnol.*, 2021, **9**, 643722.

94 S. K. Venkatraman, R. Choudhary, G. Krishnamurithy, H. R. B. Raghavendran, M. R. Murali, T. Kamarul, A. Suresh, J. Abraham and S. Swamiappan, Biomineralization, Mechanical, Antibacterial and Biological Investigation of Larnite and Rankinite Bioceramics, *Mater. Sci. Eng., C*, 2021, **118**, 111466.

95 B. Leukers, H. Gülkan, S. H. Irsen, S. Milz, C. Tille, H. Seitz and M. Schieker, Biocompatibility of Ceramic Scaffolds for Bone Replacement Made by 3D Printing, *Mater. Werkst.*, 2005, **36**, 781–787.

96 C.-H. Chang, C.-Y. Lin, F.-H. Liu, M. H.-C. Chen, C.-P. Lin, H.-N. Ho and Y.-S. Liao, 3D Printing Bioceramic Porous Scaffolds with Good Mechanical Property and Cell Affinity, *PLoS One*, 2015, **10**, e0143713.

97 R. G. Ribas, V. M. Schatkoski, T. L. Montanheiro, A. do, B. R. C. de Menezes, C. Stegemann, D. M. G. Leite and G. P. Thim, Current Advances in Bone Tissue Engineering Concerning Ceramic and Bioglass Scaffolds: A Review, *Ceram. Int.*, 2019, **45**, 21051–21061.